Exploring the Thermodynamics of the Quark-Gluon Plasma Freeze-out Hypersurface

Han Gao

Department of Physics

McGill University, Montréal

April, 2023

A thesis submitted to McGill University in partial fulfillment of the requirements of the degree of

Master of Science

Abstract

In this thesis, we present a thermal model for Quark-Gluon Plasma (QGP) freeze-out that includes an effect which mixes contributions from freeze-out points with different rapidities in observed the final particle rapidity distribution, referred to as the smearing effect. Using this model, we obtained the thermodynamic profile of the QGP freeze-out surface by fitting particle yields from a hydrodynamic simulation. By comparing it with the standard thermal model and the hydrodynamic simulation, our study reveals significant uncertainties in both thermal models when they are applied to large rapidity regions, while for mid-rapidity they both agree well with the hydrodynamic simulation. By applying it directly to experimental data, we also demonstrate the effectiveness of the smearing thermal model in constraining particle yields and thermodynamics around mid-rapidity. However, the model gives a lower temperature than the ones obtained from using thermal models on yields from hydrodynamic simulations, highlighting the need to consider feed-down effects in future studies.

Abrégé

Dans cette thèse, nous présentons un modèle thermique pour étudier le decouplace du plasma quarks-gluon avec l'effet de brouillage thermique. Nous l'appliquons en ajustant la production de particules et en comparant aux résultats de simulations hydrodynamiques. Nous étudions ses caractéristiques en comparant la thermodynamique de la surface de découplage obtenue à partir du modèle thermique brouillé, du modèle thermique standard et de la simulation hydrodynamique. Notre étude révèle des incertitudes importantes dans les deux modèles lorsqu'ils sont appliqués à des régions de grande rapidité. En l'applicant directement aux données expérimentales, nous démontrons également l'efficacité du modèle thermique brouillé pour contrôler les spectres de particules et la thermodynamique autour de la rapidité moyenne. Cependant, le modèle révèle une température inférieure à celle attendue, soulignant la nécessité de prendre en compte l'effet des désintegrations successives dans les études futures.

Acknowledgements

I would like to take this opportunity to thank my supervisor Prof. Charles Gale. I am greatly grateful to him for his supports and guidance in every aspect of my master study. I would also thank Dr. Lipei Du for sharing his ideas and our cooperation on the paper related to this thesis, and Prof. Sangyong Jeon for providing many useful insights on the research. Finally, many thanks go to Hongxing Chen for not only her support but also some technical help.

Table of Contents

List of Figures

List of Tables

Chapter 1

Introduction

1.1 Two basic properties of QCD

Quantum chromodynamics (QCD) is a theory describing the strong interaction, whose basic degrees of freedom are quarks and gluons. Quarks make up nucleons such as neutron and proton, while gluons are responsible for the force between those quarks. In other words, strong interaction is the force that holds quarks together to form nuclei, and the subject of nuclear physics is to explore various properties of QCD.

The QCD Lagrangian is

$$\mathcal{L} = \sum_f \bar{\psi}_f^i (i \not{D}_{ij} - m_f \delta_{ab}) \psi_f^j - \mathrm{tr}\, \frac{1}{2} F_{\mu\nu} F^{\mu\nu}. \tag{1.1}$$

Here ψ_f^i is quark field whose elementary excitation is a fundamental particle called quark, and it carries a colour i and a flavour f with mass m_f. $\not{D}_{ij} = \delta_{ij} \not{\partial} - ig \not{A}_{ij}$ is the covariant derivative in colour space, where g is the colour charge and A_{ij} is the gluon field, to be discussed later[1]. In the standard model (SM), there are 3 colours "charges": red, green and blue. While there are 6 flavours of quarks listed in table 1.1, for the energy scale that we are interested in[2], only 3 of them with less masses are the effective degrees of free-

[1] We have also used the Feynman slash notation $\not{a} = a_\mu \gamma^\mu$ where γ^μ are the gamma matrices [1].

[2] Namely within $\Lambda_{\mathrm{QCD}} \approx 200\ \mathrm{MeV}$, given in eq. (1.6)

Quark name	up	down	strange	charm	bottom	top
Symbol	u	d	s	c	b	t
Mass	2.2 MeV	4.6 MeV	96 MeV	1.28 GeV	4.18 GeV	173.1 GeV

Table 1.1: List of quarks in standard model with their symbols and masses. The masses given here are only approximate and with relatively large uncertainties that are not displayed here.

dom, namely up, down and strange quarks. $F^{\mu\nu}$ is the gluon field strength tensor which contains the electric and magnetic field as in the electromagnetic interaction. Therefore, gluons are generally depicted as the force carrier between quarks.

Like the gluon field strength tensor $F_{\mu\nu}$ discussed above, many concepts in QCD have their analogy in Quantum electrodynamics (QED), the theory for electromagnetic (EM) interaction. However, the most distinct and important difference of QCD from QED is that it is a non-Abelian gauge theory. This terminology is derived from language of group theory, where the group for the gauge symmetry in QCD, $SU(3)$, is non-Abelian or non-commutative, while for QED it is an Abelian group $U(1)$. Thus, the gauge field in QED A_μ takes a c-number value so commutativity holds trivially as $A_\mu A_\nu = A_\nu A_\mu$.

For QCD, the gauge field A_μ representing the to gluon is matrix-valued, and can be expanded using the 8 generators T_a of $SU(3)$ as[3]

$$A_\mu = A_\mu^a T_a. \tag{1.2}$$

Being matrices themselves, the non-commutativity of T_a's are responsible for QCD being non-Abelian.We introduce the structure constants f_{abc} to quantitatively describe non-commutativity of the generators

$$[T_a, T_b] \equiv T_a T_b - T_b T_a = i f_{abc} T_c. \tag{1.3}$$

[3]There is not a unique choice of T_a's, as long as they form a complete basis of all 3×3 traceless Hermitian matrices, and are normalized as $\mathrm{tr}\, T^a T^b = \frac{1}{2}\delta^{ab}$. In practice, they are generally chosen to be Gell-Mann matrices [10].

As a result of the non-commutativity, when constructing the field strength tensor $F_{\mu\nu}$ in eq. (1.1), instead of having $F_{\mu\nu} = \partial_\mu A_\nu - \partial_\nu A_\mu$ as it is in QED, we need to introduce a quadratic term in $F_{\mu\nu}$ so the gauge invariance in the Lagrangian is respected with

$$F^a_{\mu\nu} = \partial_\mu A^a_\nu - \partial_\nu A^a_\mu + g f_{abc} A^b_\mu A^c_\nu. \tag{1.4}$$

Here g is the QCD coupling constant, discussed later. Such a quadratic term will prove important later, as it introduces gluon self-interactions.

Deep-inelastic scattering experiments have revealed the inner structure of nucleons, which are believed to be constituted by quarks and gluons [11]. However, one of the important traits of QCD, forbids us to free any quark from nucleons. The reason can be qualitatively understood as follows. Going back to the Abelian analog QED: when one tries to pull two electrons apart, the potential energy between them decays as $1/r$; however in QCD, separating two quarks results in the potential energy between those quarks growing almost linearly, and is described by the Cornell potential [12]

$$V(r) = -\frac{4}{3}\frac{\alpha_s}{r} + \sigma r, \tag{1.5}$$

where α_s is the QCD running coupling to be given in eq. (1.6), and $\sigma \approx 0.9\,\mathrm{GeV/fm}$ is the QCD string constant, determined empirically. The linear term σr results in a very large energy density in the spatial region between those two quarks, and there is one point where the potential energy is so high that it is energetically favourable to create a new pair of quark and anti-quark out of the vacuum. Therefore, the energy invested in pulling two quarks inside a quark pair apart finally results in more quark pairs.

Another argument for the confinement comes from the running coupling constant of QCD. In the language of quantum field theory (QFT), the coupling constant describes the strength of interaction between fields[4]. In QED, the coupling constant is the electric charge of a matter particle. The charge couples the matter particle to electromagnetic

[4]Or in some cases, self-interaction.

fields, and allows it to participate in the EM interaction. In the non-Abelian gauge theory QCD, the QCD coupling constant g encodes how strongly a quark interacts with a gluon, as well as how gluons interact with themselves. One of the most interesting facts in QFT, resulting from the renormalization group [1, 13], is that the couplings, and other parameters like the particle mass, are actually not constants but they instead depend on the energy scale in which we are interested in μ. For QED, e increases slowly as we go to higher as higher energy, whereas for QCD, the coupling g is larger in the low-energy region, described as [1, 14]

$$\alpha_s(\mu) \equiv \frac{g^2}{4\pi} = \frac{2\pi N_c}{(11N_c - 2N_f)\ln(\mu/\Lambda_{\mathrm{QCD}})}. \tag{1.6}$$

Here $N_c = 3$ in standard $SU(3)$ QCD, N_f is the quark flavour number which can be

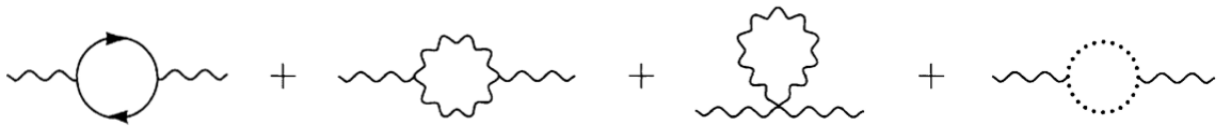

Figure 1.1: Gluon self-energy in QCD. The first diagram (virtual quark pair) has its correspondence in QED, while the rest of them are new from the non-commutativity of QCD. Here, solid lines are fermions, wavy lines are gluons, and dotted lines represent ghost particles. Figure taken from [1].

taken to be 3 when the energy scale μ is much less than charm quark mass $m_c \sim 1\ \mathrm{GeV}$, and $\Lambda_{\mathrm{QCD}} \sim 200\ \mathrm{MeV}$ is the energy scale of QCD. The distinct differences from QED are the non-Abelian nature of QCD that gives rise to the 3- and 4-gluon interaction as earlier discussed, as well as the appearance of ghost particles[5] [1, 14]. Therefore, when computing gluon self-energy responsible for the correction to the coupling g, there are three extra contributions shown in fig. 1.1.

[5]Since there are redundant degrees of freedom from gauge symmetry, when quantizing a gauge theory, introducing a gauge fixing is necessary. For $U(1)$ gauge theory, the gauge fixing doesn't contribute to any new particle nor any new interaction, while for non-Abelian gauge theory, the ghost particle is introduced by the gauge fixing and it interacts to quarks.

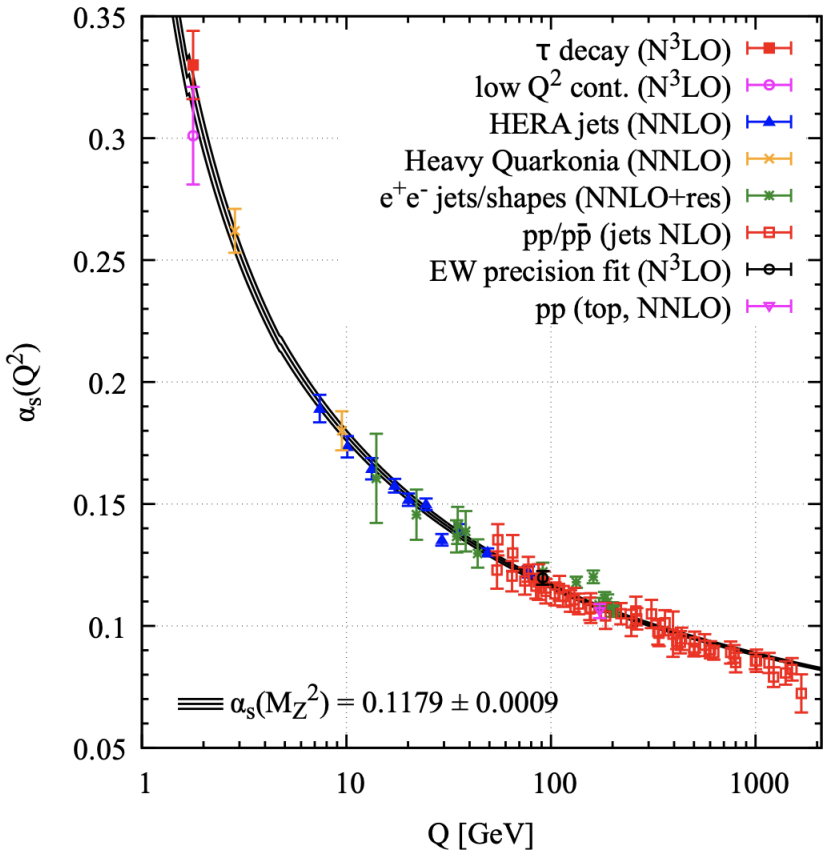

Figure 1.2: The running of coupling of QCD and its experimental measurements. The horizontal axis is for the energy scale denoted as μ in eq. (1.6). $M_Z = 91.2\,\mathrm{GeV}$ is the Z-boson mass. The legends are for different experiments and NLO,NNLO,N^{3}LO are the order of perturbation theory used in extracting α_s (e.g., NLO=next-leading-order, etc.). Figure taken from [2].

Such an energy-decreasing α_s in eq. (1.6) has been verified experimentally [2], as illustrated in fig. 1.2. As α_s increases when we move to the low energy region, the perturbation methods that are widely used in standard QFT fall, and quarks must be confined in mesons and hadrons; while in the high-energy region beyond Λ_{QCD}, α_s is small so perturbative calculations are feasible. As a result, this high-energy region is also called perturbative QCD (pQCD) region. As one goes to infinitely high energy, $\alpha_s \to 0$ so the strong interaction gradually disappears. This property, called asymptotic freedom (AF), is another important property of QCD.

Although the concepts of confinement and asymptotic freedom receive empirical support, rigorous mathematical proofs of these phenomena in QCD are still missing. Nevertheless, a large community is working on studying the macroscopic, many-body properties of QCD from an ensemble of quarks and gluons, with experimental and phenomenological methods. There are two ways to achieve this: going to high temperature or high density [3,15]. For high density, let's imagine we have a finite size box and gradually populate it with more quarks inside. Initially when the quark number is small, those quarks are energetically favoured to form a bound state, which is the hadron. However, as more and more quarks are put in, the quark wavefunctions start to overlap, as we can no longer tell one quark from another, a scenario very similar to superfluidity [16,17]. In fig. 1.3 we show a cartoon description of this scenario. In our universe, this matter is suspected to

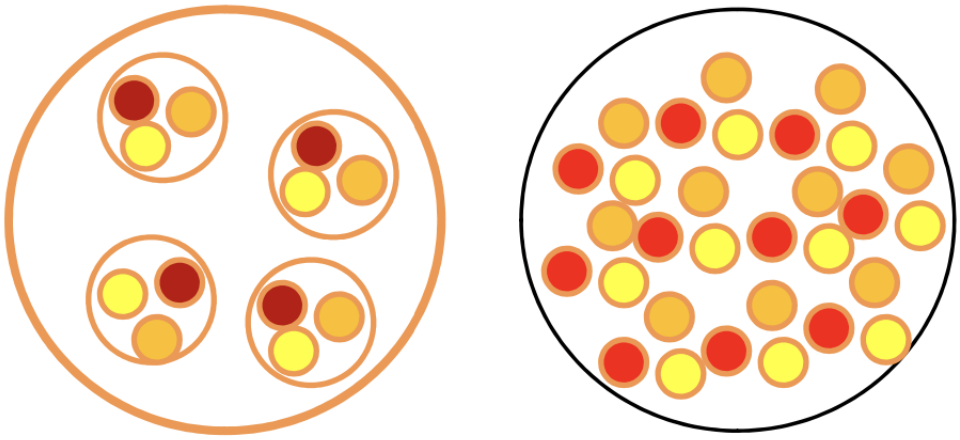

Figure 1.3: Nucleons at normal density (left) and high density (right). Figure taken from [3].

exist in the core of neutron stars [17]. On the other hand, for high temperature, let us imagine a finite-size box being heated up, quark–anti-quark ($q\bar{q}$) pairs will be excited out of the vacuum and again, when more and more quarks and anti-quarks are created their wavefunctions start to overlap. We reach a new matter of state called quark-gluon plasma (QGP). This was first predicted in the late 1970s, and a transition temperature from QGP to hadronic phase $T_c \sim 150\,\mathrm{MeV}$ was proposed [18–20]. Such high temperature can be

found when we collide two relativistic heavy-ions (heavy ion collision, HIC), or in the very early universe when the temperature was still high enough to produce QGP [21].

1.2 QCD phase diagram

As we found that hadron matter behaves in a totally new way when the density (represented by the baryon chemical potential μ_B) or temperature T is large, we would expect that there are phase transitions when we go from, for instance, deconfinement to confinement state. A brief scheme of the different phases of QCD matter plotted on the (T, μ_B) plane is the QCD phase diagram, and is qualitatively shown in fig. 1.4.

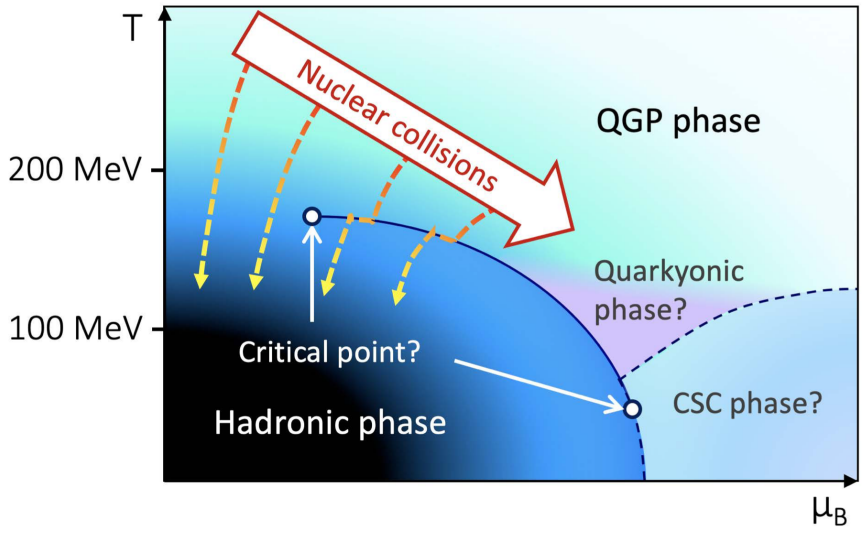

Figure 1.4: A schematic illustration of the QCD phase diagram on (T, μ_B) plane, where T is the temperature (in unit of MeV) and μ_B is the baryon chemical potential. Figure taken from [4].

In this section, we will discuss different regions on the phase diagram fig. 1.4.

1.2.1 Colour superconductivity

We start by briefly discussing the bottom-right region of the phase diagram, which is called colour superconductivity (CSC), corresponding to a high density but low temper-

ature phase. As it is suggested by its name, the idea of CSC is very similar to the electric superconductivity. In electric superconductivity, an attractive interaction between two electrons carried by a phonon lowers the free energy of the system if fermions around the Fermi surface are paired up. The pairs then act like bosons and condense [22, 23]. A similar mechanism takes place for hadron matter at low temperature but a large baryon density, where the attractive force comes from gluon exchange. The precise values of nuclear densities where CSC sets in remain unknown, but it is suspected that densities are beyond the reach of any terrestrial experiment. Therefore, the evidence of CSC has been pursued deep inside neutron stars. From low-density hadronic phase to high-density CSC phase, there is a first-order phase transition like the case for electric superconductivity, and a critical point for a higher CSC transition temperature is also speculated like the case for electric superconductivity. However no direct evidence has been found so far [17, 24].

1.2.2 Quark-gluon plasma

We come to the discussion for the top-left region of the phase diagram fig. 1.4 where the temperature is high. There, when the fireball produced in a HIC cools down, it goes from a QGP phase to a hadronic phase. However, a phase transition does not always happen: when the baryon chemical potential is low enough, the transition turns out to be a smooth cross-over [25], as confirmed by lattice QCD calculations.

Here we briefly talk about some basic facts about lattice QCD. Lattice QCD discretizes QCD on a grid and performs the path integral by summing up a large number of Monte-Carlo samplings. Lattice QCD allows us to do ab-initio nonperturbative QCD calculations to evaluate QCD thermodynamic properties. However, the notorious sign-problem [26, 27] prevents it from exploring the QCD phase diagram where baryon chemical potential μ_B is finite. Some techniques such as a Taylor expansion in μ_B are used [28] to extend lattice QCD to a small-μ_B region. Currently in the regions where lattice QCD currently works, every thermodynamic quantity still turns out to be smooth, disfavouring a phase

transition [25, 29, 30]. However, despite the lack of a genuine phase transition in lattice QCD, we indeed see a large change in the degrees of freedom in the high-temperature region, which suggests the deconfinement of nuclear matter at high energy. A pseudo-critical temperature can be defined for such a smooth cross-over from QGP to hadronic phase, which is found to be $T_{pc} \simeq 156.5\ \mathrm{MeV}$ at $\mu_B = 0$ [31].

At lower temperatures, a first order phase transition is evident in effective theories such as is the Polyakov–Nambu–Jona-Lasinio (PNJL) model [32] for large μ_B. Therefore, the presence of a critical point is speculated. Experimentally speaking, in order to search for the critical point, one has to set the system to evolve on different paths on the phase diagram (demonstrated by the dashed arrows on fig. 1.4). Efforts in varying beam energy and changing colliding nuclei have been made to set the system on different paths, a strategy called beam-energy scan. However, since QGP produced in a HIC is not homogeneous, the system can evolve differently at different spatial position, so the system can evolve along different paths on the phase diagram even for a single even of HIC, offering us more opportunities in searching for the critical point. The search for a QCD critical point is currently ongoing.

Finally before closing the section, it should be made clear that the phase diagram sketched in fig. 1.4 is far from complete, especially for the large μ_B region. For example, in the central area in fig. 1.4 marked with "Quarkyonic phase?" is another theoretically proposed dense and confined phase of QCD matter, found in large N_c expansions [33]. The evidence of a CSC phase is also being pursued. Mapping out a detailed QCD phase diagram is one of the main goals of nuclear physics.

1.3 Evolution of a fireball: Stages of a heavy ion collision

Considering the QCD phase diagram, let's move back to our discussion of the trajectories in fig. 1.4 of HIC. In this section, we give a schematic description on how the system evolves and what tools are used to describe the system at each stage.

We refer to the system produced by HIC as a "fireball", and the fireball evolution is often called a "little bang", reminiscent of the big bang in cosmology [34]. This is due to their similarities, which include not only their rapid expansion, but also many common physical mechanisms that we will later explore [15].

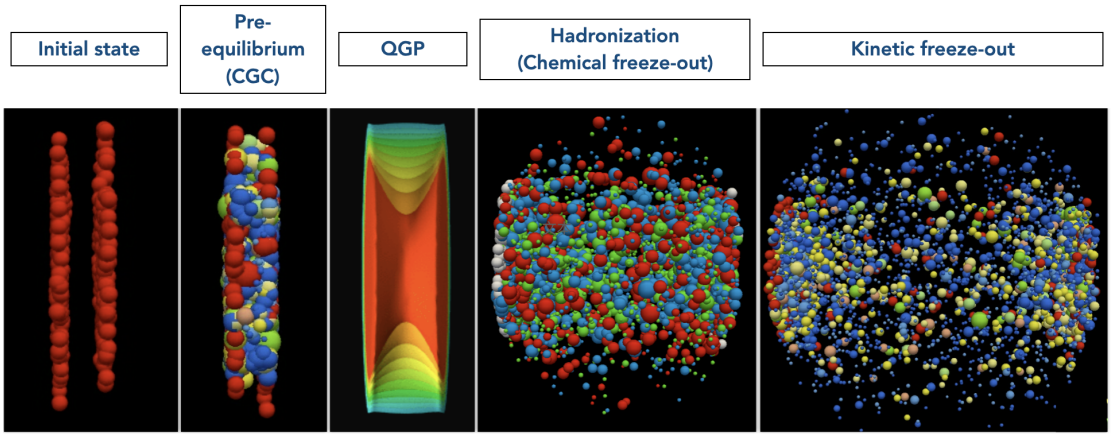

Figure 1.5: Stages of the evolution of a fireball produced in HIC. From left to right: (a) Initial state: two highly contracted nuclei collide with each other, (b) Pre-equilibrium: see main text, (c) QGP: quark-gluon plasma behaves like a fluid, (d) Hadronization: hadrons are formed from QGP, (e) Kinetic freeze-out: the system is dilute and particles fly freely to the detectors. Figure adapted from [5].

An illustration for the little bang is fig. 1.5. Initially two nuclei deformed into flat shapes because of the Lorentz contraction, as they are moving near the speed of light. At the highest energy, because the parton distribution function is gluon-dominated, a large number of far-from-equilibrium gluons are left in the region between the receeding nuclei. This pre-equilibrium stage is called the colour glass condensate (CGC) state. [35,36]. The gluon field in CGC can be treated to be coherent, and study the evolution of CGC is studied by solving the classical Yang-Mills equation derived from the QCD Lagrangian

eq. (1.1). Such a model is called IP-Glasma [37]. Quarks and anti-quarks are created as the fireball in this stage gradually moves towards thermalization.

At the end of CGC stage, the fireball is almost thermalized as the system is now close to local equilibrium[6]. The system undergoes an expansion which is well described by hydrodynamics, whose formalism will be reviewed in more detail in chapter 2. Along with its rapid hydrodynamical expansion, the QGP also cools down as its temperature approaches the QGP-hadron transition temperature T_{pc} discussed in section 1.2. At this moment what happens is hadronization or chemical freeze-out, where quarks recombine into hadrons. The chemical composition of the fireball remains almost stable after chemical freeze-out. However, the system is still close to a local equilibrium after the chemical freeze-out as the mean-free-path of the particles remains small. Therefore, hydrodynamic description remains applicable after the chemical freeze-out.

As the system continues to expand and cool, the mean-free-path of the particles will soon become larger than the system size, rendering collisions between particles unlikely: the kinetic freeze-out happens. The temperature for kinetic freeze-out to happen is found to be slightly lower than chemical freeze-out. After the kinetic freeze-out, particles fly freely to the detectors where final observables, such as the spectra and distributions of the final-state particles, are measured. The phenomenological aspect of HIC physics is therefore, mainly a study of inferring the properties of QGP from the final observables.

It is also worth mentioning that, apart from the final-state particles, electromagnetic (EM) radiation also provides valuable information. As EM interaction is 2-order-of-magnitude weaker than strong interaction ($\alpha_{EM}/\alpha_s \sim 1/100$), EM probes (photons and dileptons) which don't participate in the strong interaction, remain almostly unscathed once produced, giving information about every stage of the fireball evolution [38–40].

In conclusion, the little bang happens in a HIC highly resembles to the big bang, in both the sense of physical mechanisms and in the way data is analysed. The expanding

[6]An idealised thermalization and equilibrium can hardly be reached. In the practice of using a hydrodynamic description for the following stage, the deviation from equilibrium state manifests itself in the viscous corrections.

fireball goes through multiple stages until its final freeze-out when hadronic observables are produced.

1.4 Thermal models

Thermal models are tools to extract the thermodynamic information of the chemical freeze-out from the final spatial distribution of these hadrons. Intuitively, QGP chemical freeze-out should be close to the phase-transition line, since chemical freeze-out is by-definition where hadrons are formed out of the QGP. This is indeed true for small baryon density, but for large baryon density, the chemical freeze-out happens at a temperature below the the phase-transition line. A conclusive understanding of this feature is still lacking [41]. However the chemical freeze-out does happen very shortly after the system crosses the phase-transition line in HICs [42]. It is argued that hadron multiplicities are established very close to the phase boundary between hadronic and quark matter [43]. We would thus like to understand more on QCD phase transition by studying the QGP freeze-out. This thesis is devoted on exploring the thermodynamics of the freeze-out using different models.

Generally when experimental data on the final state particle distributions is presented, the freeze-out thermodynamics can be explored phenomenologically by running a multistage (3+1)D simulation where the QGP phase is described by relativistic hydrodynamics [44]. The detail of relativistic hydrodynamics will be reviewed in chapter 2. With final observables obtained in the experiment respected by the simulation, one can read out the freeze-out thermodynamics from the hydrodynamic simulation where the freeze-out takes place [7, 45].

However, running such a multistage simulation is costly in computation time. Thermal models, on the other hand, link directly on the freeze-out thermodynamics with the observed multiplicities (total number of a given species of particle in a little bang) and is generally cheap in computation. In addition, compared to hydrodynamic simulations,

thermal models are more physically intuitive, as their starting point is the assumption that hadrons created in a HIC form a resonance gas in equilibrium, so multiplicities are given by the equilibrium statistical distribution of a thermal source [46,47]. The history of using thermal models in subatomic physics can be traced back to the works of Fermi [48] and Landau [49] in 1950s. We will review more theoretical aspects of this approach in section 3.2.2.

The standard use of thermal models only deals with only multiplicities[7] instead of any momentum or distribution of observed particles. It can only give the thermodynamics of a single freeze-out point on the QCD phase diagram for one experiment. In order to probe more freeze-out points using the thermal model, one must vary the collision energy or the colliding nuclei. Such an effort is the beam-energy scan [50–53].

However, the fireball produced in HIC is inhomogeneous, which should exhibit aleardy different freeze-out points at different spatial locations on the freeze-out surface. Such an inhomogeneity manifest itself in the momentum distributions of the final-state particles, which are measured experimentally as discussed. It is therefore intriguing to extent the thermal model to describe an inhomogeneous freeze-out, which is one of the purposes of this thesis.

A rapidity scan [54–56] is a widely used approach in exploring the freeze-out inhomogeneity in the beam (longitudinal) direction. Here, rapidity (y) is a quantity that relates to the particle's momentum along the beam direction, to be discussed in detailed in section 3.3.1. The particle rapidity distributions $\frac{dN}{dy}$ are available from experiments like NA49 [57] and BRAHMS [8,9]. In this approach, a thermal model is used on each rapidity bin with a given width, which is $\Delta y = 0.5$ in ref. [56] for example. Each rapidity bin is treated individually to apply the thermal model used for the entire fireball.

This approach relies on the assumption that rapidity bins can be treated as independent, which is questionable because of the presence of the thermal smearing effect. The thermal smearing effect refers to the fact that a freeze-out point with a given rapidity y

[7] Or in some cases, deals with particle yields $\frac{dN}{dy}$ at mid-rapidity $y = 0$ only.

gives rise to not only final-state particles with the same rapidity y, but also a finite number of particles with rapidities near, but not equal to y. The physics of the thermal smearing effect is to be discussed in chapter 3, where we also set up a thermal model with smearing effect being taken into consideration, referred as smearing thermal model.

It is both interesting and essential to check whether smearing effect gives a significant correction in extracting freeze-out thermodynamics with rapidity scan. In addition, although the thermal models are more economic to employ than a full multistage hydrodynamic simulation, it is still necessary to check if they give consistent results. In chapter 4, we compare results in extracting freeze-out thermodynamics from thermal models with and without smearing, and also from a hydrodynamic simulation, using particle rapidity distributions obtained from the same hydrodynamic simulation [7]. We lastly use our smearing thermal model directly on the experimental data from the the BRAHMS experiment [8, 9] using a Bayesian approach in chapter 5, where we report its performance on extracting freeze-out thermodynamics with results and their uncertainties. A summary and outlook are given in chapter 6.

Chapter 2

Hydrodynamic description of QGP evolution and freeze-out

In this chapter, we give a brief review of the basic theory of viscous relativistic hydrodynamics in section 2.1 followed by a synopsis of the Cooper-Frye prescription in section 2.2. The reason of giving a review here is two-fold: first of all, relativistic hydrodynamics itself receives huge success in modeling the fireball expansion; secondly, since we will later use particle distributions that were produced by a multi-stage hydrodynamic simulation and compare the performance of thermal models and the hydrodynamic model in chapter 4, the review here is thus also for the completeness of this thesis.

2.1 Relativistic ideal and viscous hydrodynamics

Non-relativistic hydrodynamics has long been studied, and has many direct applications to almost all branches of physics from astrophysics to condensed matter physics. Another highlight of hydrodynamics is its successful engineering application, even if a thorough understanding of the turbulence problem in Navier-Stokes (NS) equations is still lacking. In modern theoretical physics, hydrodynamics is generally regarded as a low-energy effective theory with microscopic degrees of freedom (with momentum of each particle

integrated out), making macroscopic fields like fluid velocity $\vec{v}(\vec{x},t)$, density $\rho(\vec{x},t)$ and pressure $p(\vec{x},t)$ the new degrees of freedom of the theory. It is usually constructed by using the conservation law of particle number[1], energy and momentum.

In order to utilise this idea to study QGP, a relativistic version of hydrodynamics must be formulated. This can be done by the same philosophy of using conservation laws like in the non-relativistic case. In relativity, energy and momentum are collectively encoded in the energy-momentum tensor, or stress tensor $T^{\mu\nu}$, which can be directly determined from the microscopic field theory, as well as with kinetic theory. Generally, $T^{\mu\nu}$ is a symmetric tensor[2].

Let's review the construction of relativistic hydrodynamics in more detail. Throughout this thesis, we use metric $g^{\mu\nu} = \mathrm{diag}(1,-1,-1,-1)$. In a relativistic frame, one needs to be careful about the definition of flow velocity u^μ. Here we use the popular Landau frame [60] where the flow follows energy density ϵ as

$$T^{\mu\nu}u_\nu = \epsilon u^\mu. \tag{2.1}$$

Also, we required u^μ to be normalized as $u^\mu u_\mu = 1$. With u^μ defined, we can then construct a spatial projector

$$\Delta^{\mu\nu} = g^{\mu\nu} - u^\mu u^\nu, \tag{2.2}$$

which satisfies $\Delta^{\mu\nu}u_\nu = 0$. In the ideal limit, we assume $T^{\mu\nu}$ doesn't contain any term involving gradient, so the only rank-2 symmetric tensors we can use to construct $T^{\mu\nu}$ are $g^{\mu\nu}$ and $\Delta^{\mu\nu}$. Using eq. (2.1), it is realized that

$$T^{\mu\nu}_{(0)} = \epsilon u^\mu u^\nu - p\Delta^{\mu\nu}. \tag{2.3}$$

[1] For non-relativistic hydrodynamics only.

[2] It is worth noticing that it is recently realized that the anti-symmetry of $T^{\mu\nu}$ encodes spin contribution, and spin-hydrodynamics is constructed based on this fact [58,59].

By going back to the non-relativistic limit, the parameter p can be identified with the pressure of the fluid. The subscript (0) here indicates the zeroth order in gradient, as one has more available ingredients to construct $T^{\mu\nu}$ when we go higher and higher order in flow gradient. In the fluid rest frame (frf), $u^\mu = (1, \vec{0})$ and $T^{\mu\nu}_{(0)} = \mathrm{diag}(\epsilon, p, p, p)$.

Now we can proceed to implement the conservation law $\partial_\mu T^{\mu\nu} = 0$. By applying u^ν and $\Delta^{\nu\lambda}$ on both sides, we arrive at the relativistic Euler equations

$$(\epsilon + p) D u^\mu - \nabla^\mu p = 0; \tag{2.4}$$

$$D\epsilon + (\epsilon + p)\theta = 0. \tag{2.5}$$

Here $\nabla^\mu = \Delta^{\mu\nu}\partial_\nu$ is the spatial derivative, $D = u \cdot \partial$ is the comoving derivative and $\theta = \partial \cdot u$ is the scalar expansion rate of the fluid. Note that there are 5 equations in eqs. (2.4) and (2.5) but they have one redundancy since it is derived from $\partial_\mu T^{\mu\nu} = 0$ which encodes 4 equations. While the unknown fields u^μ, p, ϵ represent 5 degrees of freedom[3], eqs. (2.4) and (2.5) are not sufficient to determine the evolution of the fluid. Therefore an additional equation is needed. The equation of state serves this purpose by relating the pressure with energy density, i.e. $p = p(\epsilon)$, and it takes different forms for different substances. Note that $p(\epsilon)$ can only be found via the underlying microscopic theory, or be measured from experiments. In our practice of applying hydrodynamics to QGP, the equation of state of QCD is needed, and for the low baryon density region in the QCD phase diagram this is usually calculated with lattice QCD.

Viscous hydrodynamics involves the first order correction of eq. (2.3). Let's write $T^{\mu\nu} = T^{\mu\nu}_{(0)} + T^{\mu\nu}_{(1)} + O(\partial^2)$. Note that the Landau condition eq. (2.1) is already satisfied by $T^{\mu\nu}_{(0)}$, thus $T^{\mu\nu}_{(1)}$ needs to be transversal to u^μ, i.e. $T^{\mu\nu}_{(1)} u_\nu = 0$. The only available ingredients involving the first-order gradients are $\partial^\mu u^\nu$, $u^\mu D u^\nu$ and θ. Let's decompose $T^{\mu\nu}_{(1)}$ by $\Delta^{\mu\nu}$ as

$$T^{\mu\nu}_{(1)} = -\Pi \Delta^{\mu\nu} + \pi^{\mu\nu}, \tag{2.6}$$

[3]Since u^μ is normalized as $u^\mu u_\mu = 1$, it has only 3 degrees of freedom.

With eq. (2.6), the conservation law reads

$$\partial^\nu \epsilon - \Delta^\nu (p + \Pi) + (\theta + D)(p + \Pi) u^\nu + \partial_\mu \pi^{\mu\nu} = 0, \tag{2.7}$$

which encodes the relativistic NS equations. Before going to the discussion on the relativistic NS equations, let's first take a look into the viscous correction Π and $\pi^{\mu\nu}$ in more details.

We first explore the possible tensor composition of Π and $\pi^{\mu\nu}$. Based on the previous discussion, they should contain and only contain the first-order derivatives of u^μ, and $\pi^{\mu\nu}$ should be perpendicular to both u^μ and $\Delta^{\mu\nu}$. Let $\pi^{\mu\nu} \propto \frac{1}{2}(\partial^\mu u^\nu + \partial^\nu u^\mu) + \frac{b}{2}(u^\mu D u^\nu + u^\nu D u^\mu) + c\Delta^{\mu\nu}$ with symmetric indices respected. Acting with u_μ on both sides gives $b = -1$ and acting with $\Delta^{\mu\nu}$ yields $c = -1/3$. Also, since Π is a scalar and is of $O(\partial)$, it can only depend linearly on θ. Therefore, we parameterize

$$\Pi = -\zeta\theta, \quad \pi^{\mu\nu} = 2\eta\partial^{\langle\mu} u^{\nu\rangle}, \tag{2.8}$$

where $\pi^{\mu\nu}\Delta_{\mu\nu} = 0$ and $\pi^{\mu\nu}u_\nu = 0$. The $^{\langle\mu\nu\rangle}$ symbol is defined as

$$\nabla^{\langle\mu} u^{\nu\rangle} = \frac{1}{2}(\partial^\mu u^\nu + \partial^\nu u^\mu) - (u^\mu D u^\nu + u^\nu D u^\mu) - \frac{1}{3}\Delta^{\mu\nu}\theta \tag{2.9}$$

The way we parameterized Π and $\pi^{\mu\nu}$ can be rationalized by using an entropy analysis, which also highlights the reason why we named them viscous corrections. The first law of thermodynamics for a fluid cell is

$$d\epsilon = T ds, \tag{2.10}$$

where T is the temperature and s is the entropy density. We recognize entropy flow as $s^\mu = s u^\mu$. The second law of thermodynamics requires that entropy is always increasing,

so

$$\partial_\mu s^\mu = \theta s + Ds \geq 0, \tag{2.11}$$

Using eq. (2.10), $Ds = \beta D\epsilon$. Here $\beta = 1/T$ stands for the inverse temperature. Multiplying u_ν on both sides of eq. (2.7) yields

$$D\epsilon = -(p + \epsilon + \Pi)\theta - u_\nu \partial_\mu \pi^{\mu\nu} = -(p + \epsilon + \Pi)\theta + \pi^{\mu\nu}\partial_\mu u^\nu, \tag{2.12}$$

inserting into eq. (2.11) yields

$$T\partial_\mu s^\mu = (Ts - p - \epsilon)\theta - \Pi\theta + \pi^{\mu\nu}\partial_\mu u_\nu \geq 0. \tag{2.13}$$

The first term $(Ts - p - \epsilon)\theta$ is the contribution from ideal hydrodynamics and should be zero since we assume ideal hydrodynamics is non-dissipative. This allows us to recognize $Ts = p + \epsilon$. The second term $-\Pi\theta$ is positive semi-definite if and only if $\Pi = -\zeta\theta$ with $\zeta \geq 0$. Finally for the last term, using the fact that $\pi^{\mu\nu}$ is a symmetric tensor, we can rewrite is as $\pi^{\mu\nu}\partial_{(\mu}u_{\nu)}$. Then use the fact that $\pi^{\mu\nu}u_\mu$ and $\pi^{\mu\nu}\Delta_{\mu\nu} = 0$, we find that this term can be also writeen as $\nabla^{\langle\mu}u^{\nu\rangle}\pi_{\mu\nu}$. Since $\pi_{\mu\nu} = 2\eta\nabla_{\langle\mu}u_{\nu\rangle}$, this term is only positive semi-definite if and only if $\eta \geq 0$. Therefore, the parameterization in eq. (2.8) is justified.

Π and $\pi^{\mu\nu}$ contain the bulk and shear viscosity, ζ and η, respectively. The bulk viscosity scalar Π serves as an additional part of the pressure p, which is the correction from fluid expansion. Bulk viscosity can be related to microscopic nonequilibrium processes where energies are transferred between translational motion and the inner structure of the fluid particles, causing a correction to the macroscopic pressure [61].

On the other hand, shear viscosity can be understood as the friction between different fluid layer, as momentum is transferred by particles diffusing in and out of each layer. See fig.2.1 for an illustration. In detail, let's explore a simple case where the fluid has velocity field $u^\mu = \gamma(z)(1, v(z), 0, 0)$ where $\gamma(z) = \frac{1}{\sqrt{1-v^2(z)}}$. The entropy production rate for this

fluid velocity is

$$\dot{s} = \eta \frac{\left(\frac{dv}{dz}\right)^2}{1 - v^2} \simeq \eta \left(\frac{dv}{dz}\right)^2 . \tag{2.14}$$

In the language of thermodynamics, this is the entropy produced when there are different fluid velocities for different fluid layers, and can thus be thought as friction between the relative motion between two adjacent fluid layers.

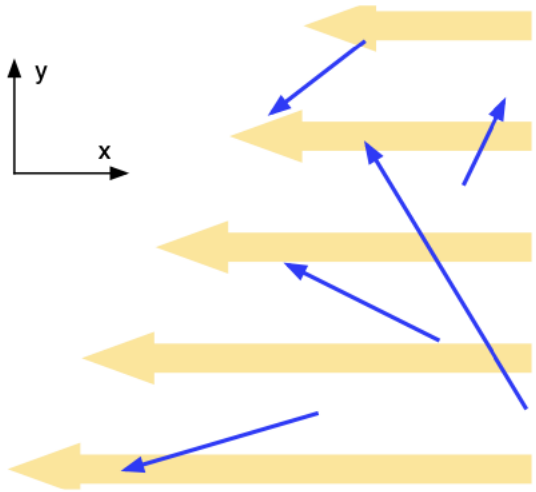

Figure 2.1: A stationary flow when velocities in each layer are different. Exchanged momentum between nearby layers leads to a macroscopic friction known as shear viscosity. Figure adapted from [6].

There are many attempts from both theory and phenomenology to find the coefficients ζ and η for QGP. On the theoretical side, the approaches include pQCD and AdS/CFT correspondence [62]. One of the most significant findings in QGP is its small shear viscosity. In 2004, using AdS/CFT correspondence and Kubo formula, Kovtun, Son and Starinets related the shear viscosity with the graviton absorption cross-section, and found a universal value for shear viscosity to entropy density ratio for a certain class of quantum field theory [63] called $\mathcal{N} = 4$ super Yang-Mills theory [64], which is

$$\frac{\eta}{s} = \frac{\hbar}{4\pi k_B}. \tag{2.15}$$

They further speculated that this value is a universal lower bound for shear viscosity of any fluid, known as the KSS bound. Although QCD doesn't fall into the class of $\mathcal{N} = 4$ super Yang-Mills theory where the universal value holds, it was later confirmed in 2010 that QGP produced by Au+Au collision at $200\ \mathrm{GeV}$ almostly saturates the KSS bound [65], where the authors found

$$1.0 \leq \left(\frac{\eta}{s}\right)_{QGP} / \frac{\hbar}{4\pi k_B} \leq 2.5, \tag{2.16}$$

where, as a comparison, for water under daily condition, its η/s is ~ 380 times greater than the KSS bound. This suggests that the QGP is "the most ideal fluid" that is known. Later studies constrain the η/s for QGP to be even closer to the KSS bound [66].

One should be aware of a common misconception that a small viscosity of a fluid indicates a weak interaction of the underlying microscopic particles. The opposite is actually true. From the kinetic theory of a dilute gas, $\eta \sim n l_{\mathrm{mfp}} \langle p \rangle$ where n is the particle number density, $l_{\mathrm{mfp}} \sim \frac{1}{n\sigma}$ is the mean-free-path of a particle, with σ being the cross section. $\langle p \rangle \sim T$ is the mean momentum of a relativistic particle. For an ideal gas, the viscosity is in fact very large due to a large l_{mfp}. In relativistic cases where the mass of a particle is negligible, $s \sim n \sim T^3$. We finally reach the estimation

$$\frac{\eta}{s} \sim T l_{\mathrm{mfp}}. \tag{2.17}$$

A small η/s thus tells a small l_{mfp}, or equivalently a large cross-section σ [67]. Therefore, such measured small η/s for QGP suggests that QGP is a strongly coupled system.

There is also a holographic study on bulk viscosity, where it is found that $\zeta/\eta = 2(1/3 - c_s^2)$ [68] with c_s being the speed of sound. This value is much larger than pQCD calculation [69] where $\zeta/\eta = 15(1/3 - c_s^2)^2$. As $c_s^2 = 1/3$ is the conformal limit, these results suggest one nature of bulk viscosity is that QGP deviates being conformal due to microscopic interactions [62].

Having discussed the physics of viscous term Π and $\pi^{\mu\nu}$, we now go back to eq. (2.7) and derive the relativistic NS equations. One of them, eq. (2.12), actually has already

appeared when discussing entropy production rate. Another one can be obtained by multiplying $\Delta_{\mu\nu}$ on both sides of eq. (2.7), then

$$(\epsilon + p - \zeta\theta)Du^{\mu} - \Delta^{\mu}(p - \zeta\theta) + 2\Delta^{\mu}_{\nu}\partial_{\rho}(\eta\partial^{\langle\nu}u^{\rho\rangle}) = 0. \tag{2.18}$$

Eqs.(2.12) and (2.18) constitute relativistic NS equations. Relativistic viscous hydrodynamics has enormous success in describing the expanding fireball. It is also worth noticing that the first order viscous hydrodynamics suffers from the well-known causality problem, where a superluminal (i.e., faster-than-light) propagation is found [70]. The popular solution to this problem is to go to the second order, which gives Israel-Stewart theory [71]. This is also the theory used later by the hydrodynamic simulation [7] related to this thesis. It is also worth mentioning that because of the ambiguity in defining temperature, velocity and chemical potential in first order hydrodynamics, adopting a frame other than the Landau frame eq. (2.1) can also solve the causality problem [72].

2.2 The Cooper-Frye prescription for particle distribution

As the QGP expands, there will be a point where the system is so dilute that particles are too far apart to interact. More quantitatively, the mean-free-paths of the particles are comparable or even larger than the system size. This point is the so-called kinetic freeze-out discussed in chapter 1. For simplicity, since we will only talk about kinetic freeze-out in this section, we hereafter simply refer it by freeze-out. At the moment of freeze-out, hydrodynamic description breaks down. After this, particles such as protons and pions fly freely to the detectors, where particle distributions are measured. Therefore, it's useful to link the hydrodynamic description to the final particle distribution. Such a link was made by Fred Cooper and Graham Frye [73].

We now briefly summarize the Cooper-Frye prescription for freeze-out. Hydrodynamic simulations usually use Milne (τ, x, y, η) coordinates, which are defined as

$$\eta = \frac{1}{2}\ln\frac{t+z}{t-z}, \tau = \sqrt{t^2 - z^2}. \tag{2.19}$$

Here, η is space-time rapidity, and τ is the proper time. Equivalently,

$$t = \tau\cosh\eta, z = \tau\sinh\eta. \tag{2.20}$$

The freeze-out surface is formally a hyper-surface in 3+1D space-time. In terms of Milne coordinates, the freeze-out surface can be written as [3]

$$\sigma^\mu = (\tau_f(x,y)\cosh\eta, x, y, \tau_f(x,y)\sinh\eta), \tag{2.21}$$

which gives

$$d\sigma^\mu = (\cosh\eta, -\partial_x\tau_f, \partial_y\tau_f, -\sinh\eta)\tau_f dxdyd\eta. \tag{2.22}$$

On the other hand, the current j_s^μ of particle species s is related by its phase-space distribution function $f_s(x,p)$ by

$$j_s^\mu(x) = \int \frac{1}{E_{\vec{p}}}\frac{d^3\vec{p}}{(2\pi)^3} f_s(x,p)p^\mu. \tag{2.23}$$

Here $\frac{1}{E_{\vec{p}}}\frac{d^3\vec{p}}{(2\pi)^3}$ is the relativistic invariant measure in 3D momentum space. We can find the particle number given by

$$N_s = \int d\sigma^\mu \int \frac{1}{E_{\vec{p}}}\frac{d^3\vec{p}}{(2\pi)^3} f_s(x,p)p_\mu, \tag{2.24}$$

from which the particle momentum distribution at freeze-out can be obtained

$$\frac{d^3N_s}{d^3\vec{p}} = \frac{1}{(2\pi)^3}\int \frac{1}{E_{\vec{p}}} d\sigma^\mu p_\mu f_s(x,p). \tag{2.25}$$

In comparison with standard formula for particle distribution function in momentum space $\frac{d^3N_s}{d^3\vec{p}} = \frac{1}{(2\pi)^3}\int d^3\vec{x} f_s(\vec{x},\vec{p})$, we recognise that $d^3\vec{x} = \frac{1}{E_{\vec{p}}} d\sigma^\mu p_\mu$. In other words, $\frac{1}{E_{\vec{p}}} d\sigma^\mu p_\mu$ plays the role of volume element. To see this more clearly, we parametrise p^μ by transversal mass m_T and rapidity y defined in section 3.3.1 so $p^\mu = m_T(\cosh y, u_x, u_y, \sinh y)$[4], we have

$$\frac{1}{E_{\vec{p}}} p_\mu d\sigma^\mu = \frac{1}{\cosh y}(\cosh(y-\eta) - u_x\partial_x\tau_f - u_y\partial_y\tau_f)\tau_f dx dy d\eta, \tag{2.26}$$

which has the dimension of volume.

In general, $f_s(x,p)$ includes equilibrium distribution and viscous corrections, i.e.

$$f_s(x,p) = f_{s,eq}(\frac{u(x)\cdot p - \mu(x)}{T(x)}) + \delta f(x,p), \tag{2.27}$$

where $f_{s,eq}$ is the Fermi-Dirac or Bose-Einstein distribution. In ideal hydrodynamics, local equilibrium is well established so $f_s(x,p) = f_{s,eq}(\frac{u(x)\cdot p-\mu(x)}{T(x)})$. Therefore, $\delta f \sim O(\partial)$ and encodes viscous correction. The relation between $\Pi, \pi^{\mu\nu}$ and δf can be obtained by Grad's 14 moments method or using the Chapman–Enskog expansion [74, 75]. The framework of Cooper-Frye prescription thus provides us a bridge between hydrodynamic simulation and the momentum distributions of final-state particles, which are measurable in experiments.

[4]Normalized by $u_x^2 + u_y^2 = 1$.

Chapter 3

Thermal Models

In this chapter, we present the theoretical foundation of thermal models used later. We start by a brief review of the thermodynamics and particle distribution function in a grand canonical ensemble in section 3.1, which later leads to the single source model (which is generalized to the discrete thermal model in section 3.4). We then give also a review of the relativistic kinematics with an emphasis on rapidity and its relevant concepts in section 3.3, and finally how to use it to construct smearing thermal model in section 3.4.

3.1 Thermodynamics of a grand canonical ensemble

A grand canonical ensemble (GCE) describes a situation where the system is connected to a bath from which the system can exchange both particles and energy. Note that for a canonical ensemble, only energy is exchanged. The system is then described by a temperature T, a chemical potential μ[1], and a volume V. The GCE is therefore useful when the particle number of the system changes naturally, like in a HIC where a large number of quarks and gluons are created from the vacuum, or when quantum statistics are involved, where the particle number is not a number but a operator without a specific pre-defined value.

[1] If multiple particle species are involved, multiple chemical potentials μ_i are correspondingly needed.

For a system with Hamiltonian $\hat{H}$, and particle number operator $\hat{N}$, the grand partition function $\mathcal{Z}$ is defined as

$$\mathcal{Z} = \operatorname{tr} e^{-\beta(\hat{H}-\mu\hat{N})}, \tag{3.1}$$

where $\beta = 1/T$ is the inverse temperature. It is clear that, from this definition, the expectation of particle number is

$$\langle \hat{N} \rangle = \frac{1}{\mathcal{Z}} \operatorname{tr}(\hat{N} e^{-\beta(\hat{H}-\mu\hat{N})}) = \frac{\partial \ln \mathcal{Z}}{\partial(\beta\mu)}. \tag{3.2}$$

Let's now consider the statistics of a single energy level given by Hamiltonian $\hat{H} = \omega\hat{N}$. Here $\hat{N}$ is the particle number operator with eigenstates $|n\rangle$. Given different natures of the particles in the system, n ranges from 0 to infinity for bosons, and takes only 0 and 1 for fermions because of the Pauli exclusion principle. For a fermionic system, we can easily compute eq. (3.1) as

$$\mathcal{Z} = 1 + e^{-\beta(\omega-\mu)}, \tag{3.3}$$

while a bosonic system requires a little algebra:

$$\mathcal{Z} = \sum_{n=0}^{\infty} e^{-n\beta(\omega-\mu)} = \frac{1}{1 - e^{-\beta(\omega-\mu)}}. \tag{3.4}$$

One should notice that in order to make the series converge, we assumed $\omega > \mu$. Such a converging condition is essential in the realisation of the Bose-Einstein condensation happening when $\omega \to \mu$ [76].

With the results above, we can now determine the average particle number occupying the energy level ω, using eq. (3.2). One finds,

$$\langle N \rangle = \begin{cases} f_B(\omega) \equiv \frac{1}{e^{\beta(\omega-\mu)}-1}, & \text{Boson;} \\ f_F(\omega) \equiv \frac{1}{e^{\beta(\omega-\mu)}+1}, & \text{Fermion,} \end{cases} \tag{3.5}$$

where $f_B(\omega)$ and $f_F(\omega)$ are the Bose-Einstein (BE) and Fermi-Dirac (FD) distribution function respectively.

In the limit $\beta(\omega-\mu) \gg 1$, the two distribution functions both reduce to the well-known Maxwell-Boltzmann (MB) distribution of classical statistics

$$f_C(\omega) = e^{-\beta(\omega-\mu)}. \tag{3.6}$$

Here the subscript C stands for classical. In the intermediate temperature region, a series expansion can be used to replace $f_{F/B} = \frac{1}{e^{\beta(\omega-\mu)}+\theta}$. Here $\theta = 1$ for fermion and -1 for boson. Again, assuming $\omega - \mu > 0$, one has

$$f_{F/B}(\omega) = \frac{e^{-\beta(\omega-\mu)}}{1+\theta e^{-\beta(\omega-\mu)}} = \sum_{n=1}^{\infty}(-\theta)^{n-1}e^{-n\beta(\omega-\mu)}, \tag{3.7}$$

or

$$f_{F/B}(\omega) = \sum_{n=1}^{\infty}(-\theta)^{n-1}f_C^{T\to T/n}(\omega). \tag{3.8}$$

Since most thermodynamic quantities depends linearly on the distribution function $f(\omega)$, this expansion allows us to write their quantum statistics as a summation of many independent classical results with temperature replaced by $T \to T/n$. It is also worth noticing that this technique is not related to the Matsubara summation in finite-temperaure field theory, nor the trace operation in eq. (3.1).

3.2 Particle numbers from a single source

3.2.1 Particle number of a relativistic ideal quantum gas

Classical statistics

For simplicity, we consider a box of non-interacting particles in the GCE. When temperature is high, the average kinetic energy of a particle becomes comparable with its mass so

the non-relativistic dispersion $E = \frac{\vec{p}^2}{2m}$ can no longer be used and must be replaced by the relativistic dispersion

$$E = \sqrt{\vec{p}^2 + m^2}. \tag{3.9}$$

For a particle in a box with size $V = L^3$, we can impose periodic boundary condition on the single particle wavefunction $\psi \sim e^{i\vec{k}\cdot\vec{x}}$, using $\psi(x, y, z) = \psi(x + L, y, z)$. It can be realised that

$$e^{ik_x L} = 1 \quad \Rightarrow \quad k_x = \frac{2\pi n_x}{L}, n_x = \ldots, -1, 0, 1, 2, \ldots. \tag{3.10}$$

In this case we say that the x-momentum k_x is quantized by a quantum number n_x. Same condition is also to be imposed on k_y and k_z. Therefore, a particle in a non-interacting gas has energy level given by

$$E_{\vec{k}} = \sqrt{\vec{k}^2 + m^2}, \quad \vec{k} = \frac{2\pi}{L}\vec{n}. \tag{3.11}$$

Recalling that eq. (3.6) gives the average number of particles occupying a quantum state with energy ω in classical statistics, we find that the total particle number in the box is

$$N_C(T, V, \mu) = \sum_{\vec{k}} g_s f_C(E_{\vec{k}}) = g_s e^{\beta\mu} \sum_{\vec{k}} e^{-\beta\sqrt{\vec{k}^2+m^2}}. \tag{3.12}$$

Here, g_s denotes the internal degree of freedom of the particle including spin, colour, etc. To examine $N_C(T, V, \mu)$ further, we work in the thermodynamic limit where $L \to \infty$, which allows us to replace the summation by an integral using

$$\sum_{\vec{k}} \to \int \frac{d^3\vec{k}}{(2\pi/L)^3} = V \int \frac{d^3\vec{k}}{(2\pi)^3}. \tag{3.13}$$

Here, $d^3\vec{k}$ is the volume element in $\vec{k}$-space, and $(2\pi/L)^3$ is the volume in $\vec{k}$-space occupied by one quantum state given by the quantization condition eq. (3.11). Now eq. (3.12) can be evaluated by using spherical coordinates

$$N_C(T, V, \mu) = \frac{g_s V}{2\pi^2} e^{-\beta\mu} \int dk\, k^2 e^{-\beta\sqrt{k^2+m^2}} = \frac{g_s VT}{2\pi^2} e^{\beta\mu} m^2 K_2(\beta m), \tag{3.14}$$

where $K_2(x)$ is the Bessel function of the second kind.

Quantum statistics

As we will see later that for some particles in the QGP freeze-out, MB approximation is less valid and quantum statistics must be used, it is useful to also derive the equations for particle numbers in quantum statistics.

Since the LHS of eq. (3.12) depends linearly on distribution function f, we can use eq. (3.8) to write the particle number as a series of classical results. Namely, for fermions,

$$\begin{aligned} N_F(T,V,\mu) &= V\sum_{\vec{k}} f_{FD}(\sqrt{m^2+\vec{k}^2}) = V\sum_{n=1}^{\infty}(-1)^{n-1}\sum_{\vec{k}} f_C^{T\to T/n}(\sqrt{m^2+\vec{k}^2}) \\ &= \sum_{n=1}^{\infty}(-1)^{n-1}N_C(T/n,V,\mu), \end{aligned} \tag{3.15}$$

substituting in eq. (3.14) yields

$$N_F(T,V,\mu) = \frac{g_s VT}{2\pi^2}\sum_{n=1}^{\infty}\frac{(-1)^{n-1}}{n}e^{n\beta\mu}m^2K_2(n\beta m). \tag{3.16}$$

Similarly for bosons,

$$N_B(T,V,\mu) = \frac{g_s VT}{2\pi^2}\sum_{n=1}^{\infty}\frac{1}{n}e^{n\beta\mu}m^2K_2(n\beta m). \tag{3.17}$$

3.2.2 From particle numbers to thermodynamics

Our task is to infer the thermodynamic properties of a fireball produced in a heavy ion collision from the particle numbers of different species. Pions, kaons and (net)-protons are easily measured. For protons, their mass is $m_p = 937\ \mathrm{MeV}$, which is much greater than the typical freeze-out temperature of the QGP $T_{FO} \sim 150\ \mathrm{MeV}$, so a classical approximation can be used. However mesons are generally lighter. For what we are interested in, pions

have mass $m_\pi = 139\ \mathrm{MeV}$ and for kaons $m_K = 498\ \mathrm{MeV}$. As their masses are comparable to the temperature, quantum statistics are required to ensure accuracy.

First, we notice that pions and kaons have zero baryon number so it has no baryon density dependence. In this case N^π and N^K depends only on temperature and volume. Especially, from eq. (3.17) the ratio N^π/N^K is uniquely determined by temperature[2]

$$\pi\text{-K ratio}(T) = \frac{N_\pi(T,V)}{N_K(T,V)} = \frac{m_\pi^2}{m_K^2}\frac{\sum_{n=1}^{\infty}(-1)^{n-1}K_2(nm_\pi/T)}{\sum_{n=1}^{\infty}(-1)^{n-1}K_2(nm_K/T)}. \tag{3.18}$$

The functional dependence of the π-K ratio on T can be numerically determined from eq. (3.18). Inverting it, we can get temperature as a function of the ratio as fig. 3.1.

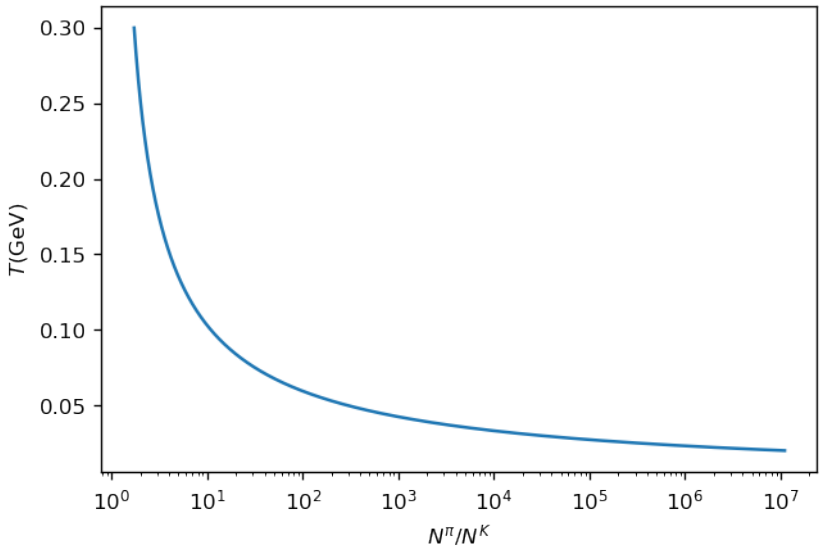

Figure 3.1: Determining temperature from the π-K ratio

[2]To avoid confusion, in this thesis, we use N with a subscript for particle number to describe its functional dependence on thermodynamics (T, μ, V) given by eqs. (3.14), (3.16) and (3.17). For example, $N_\pi(T, \mu, V)$ denotes the pion number in a GCE with (T, μ, V) given. N with a superscript is reserved for particle number as the model input without immediately knowing the thermodynamics of the system. For example, N^π represents the measured value of pion number in an experiment. In practice of this thesis, this can be also obtained from hydrodynamic simulations.

Once temperature is determined, using the fact that particle numbers are proportional to the volume of the fireball V, which can be read out as

$$V = \frac{N^{\pi}}{N_{\pi}(T, V = 1\ \mathrm{fm}^3)}\ \mathrm{fm}^3. \tag{3.19}$$

Finally, let us discuss the determination of the baryon chemical potential μ. In experiments, we usually only see the net proton number, which is

$$N_{p-\bar{p}}(T, V, \mu) = N_p(T, V, \mu) - N_{\bar{p}}(T, V, \mu) = N_p(T, V, \mu) - N_p(T, V, -\mu). \tag{3.20}$$

Here, $\bar{p}$ stands for anti-proton, and we used the fact that its chemical potential is opposite to the proton chemical potential. Using the classical statistics eq. (3.14), we can rearrange it into

$$N_{p-\bar{p}}(T, V, \mu) = (e^{\beta\mu} - e^{-\beta\mu}) N_p(T, V, \mu = 0) = 2N_p(T, V, \mu = 0) \sinh \beta\mu. \tag{3.21}$$

In the small chemical potential limit where $\beta\mu \ll 1$, the net proton number is roughly proportional to μ, so baryon chemical potential and baryon density are sometimes used interchangeably.

Eq. 3.21 can also be recast into a form involving $N_{p-\bar{p}}$ only

$$N_{p-\bar{p}}(T, V, \mu) = \frac{\sinh \beta\mu}{\sinh 1} N_{p-\bar{p}}(T, V, \mu = T), \tag{3.22}$$

from which we can determine chemical potential directly as

$$\mu = T \sinh^{-1} \frac{N^{p-\bar{p}} \sinh 1}{N_{p-\bar{p}}(T, V, \mu = T)}. \tag{3.23}$$

3.3 Rapidity distribution

3.3.1 Rapidity

To introduce the concept of rapidity, we first have a quick review of relativistic kinematics. For a particle with mass m, its energy is given by

$$E_{\vec{p}} = \sqrt{m^2 + \vec{p}^2}, \tag{3.24}$$

where $\vec{p}$ is its 3-momentum. We also use 4-momentum

$$p^\mu = (E_{\vec{p}}, \vec{p}), \tag{3.25}$$

which is normalized as $p^\mu p_\mu = m^2$.

If we choose particle to be moving along z direction, i.e. $\vec{p} = p\vec{e}_z$, we can define rapidity y such that

$$E_{\vec{p}} = m\cosh y, p = m\sinh y. \tag{3.26}$$

This parametrisation ensures the kinematics $E^2 - p^2 = m^2$ by identity $\cosh^2 y - \sinh^2 y = 1$. A particle at rest ($p = 0$) has $y = 0$. In the non-relativistic limit, $y \ll 1$ must hold so $p \ll m$ is ensured, then, by comparing the non-relativistic expression $p = mv$ where v is the velocity of the particle, it can be realised that $v \simeq y$. Therefore, rapidity can be regarded as a generalization of velocity in a relativistic setting.

In general, however, we would define z direction other than the direction in which the particle is moving. For example, in HIC, a large number of final-state particles move in different directions, while z is generally defined by the beam direction. Nevertheless a rapidity y can still be defined in this case, along with another quantity called transverse mass m_T. More precisely, we define $\sqrt{p_x^2 + p_y^2}$ as the transverse momentum p_T, then

$$m_T = \sqrt{m^2 + p_T^2}. \tag{3.27}$$

It is straight forward to show that the energy of this particle is given by

$$E_{\vec{p}} = \sqrt{m^2 + p_T^2 + p_z^2} = \sqrt{m_T^2 + p_z^2}. \tag{3.28}$$

Therefore, we can again define rapidity y by

$$E_{\vec{p}} = m_T \cosh y, \quad p_z = m_T \sinh y. \tag{3.29}$$

3.3.2 Rapidity addition

One important and useful property of rapidity is its additivity, which states that, if we have an particle moving in frame S with a rapidity y and we observe it in another frame S' where frame S is moving[3] with rapidity η. Such change of frame is defined as boost. After the boost, the rapidity of the particle will simply become $y + \eta$. One way to prove this is to use the Lorentz formula of velocity superposition in special relativity. To prove this, recall that if we have an object moving with a velocity v and its reference frame S is moving in the same direction with a velocity of u relative to another frame S', then in S' the velocity of the particle is given by Lorentz transformation

$$v' = \frac{u + v}{1 + uv}. \tag{3.30}$$

This formula ensures that the speed of the object cannot exceed speed of light in any reference frame. Now, notice that the definition of rapidity eq. (3.26) can be written as

$$\frac{p}{E_p} = \tanh y. \tag{3.31}$$

[3]Assume the particle's velocity is parallel to the velocity of frame S viewed from S', i.e., only motions along the same axis are involved.

We recongise the left hand side as the velocity of a particle. There, plugging in $v = \tanh y$ and $u = \tanh \eta$, we have

$$v' = \frac{\tanh \eta + \tanh y}{1 + \tanh y \tanh \eta} = \tanh(y + \eta), \tag{3.32}$$

which states that the rapidity for v' is nothing but $y + \eta$. This can be regared as a generalisation of the Galilean transformation.

In the modern language of special relativity, such change of reference frame is called boost, and η is its boost parameter. Thus, eq. (3.32) simply states that the rapidity of a particle after boosting is its initial rapidity plus boost parameter. In the sense of this addition law eq. (3.32) and its low-speed limit $y \simeq v$, rapidity is the relativistic generalization of the velocity as previously mentioned.

3.3.3 Space-time rapidity

In hydrodynamic simulations running on a space-time lattice, it is generally easier to deal with space-time rapidity η_s, which is not defined by the particle's momentum and energy but by it's coordinates (z, t) as defined in sect. 2.2. Also in hydrodynamic simulations, coordinates (η_s, τ) are used while the thermal model with smearing effect (to be discuss later) is formulated with rapidity y. Therefore, in order to relate two models, we need to study the relation between a fluid cell's[4] y and η_s.

To formulating such a relation, we assume that information of $\tau u^\eta \equiv \frac{d\eta_s}{ds}$, the η_s component of a fluid cell's velocity, can be obtained from hydrodynamic simulation as a function of the fluid cell's η_s coordinate. Physically, in a hydrodynamic simulation of the fireball, τu^η represents the longitudinal flow of a fluid cell.

[4]Here we only use the relation for fluid cells, but it generally applies for any object. In hydrodynamic simulation, one fluid cell at the freeze-out is a freeze-out point.

From the definition of (η_s, τ) in terms of (z, t), we have

$$\begin{pmatrix} dt \\ dz \end{pmatrix} = \begin{pmatrix} \cosh\eta_s & \tau\sinh\eta_s \\ \sinh\eta_s & \tau\cosh\eta_s \end{pmatrix} \begin{pmatrix} d\tau \\ d\eta_s \end{pmatrix}. \tag{3.33}$$

Then the invariant interval in (η_s, τ) coordinates can be written as

$$ds^2 = dt^2 - dz^2 = d\tau^2 - \tau^2 d\eta_s^2, \tag{3.34}$$

and identifying ds^2 as the proper time of the fluid cell, we have the normalization

$$u^\tau \equiv \frac{d\tau}{ds} = \sqrt{1 + (\tau u^\eta)^2}. \tag{3.35}$$

We notice that rapidity y can be written in a similar way like η_s as

$$y = \frac{1}{2}\ln\frac{E + p^z}{E - p^z}. \tag{3.36}$$

Using the definition of $v^z = \frac{p^z}{E}$, we have

$$y = \frac{1}{2}\ln\frac{1 + v^z}{1 - v^z}. \tag{3.37}$$

By using v^z defined in (z, t) coordinates $v^z = \frac{dz}{dt}$, from eq. (3.33) we recognize

$$v^z = \frac{\tanh\eta_s d\tau + \tau d\eta_s}{d\tau + \tau\tanh\eta_s d\eta_s}. \tag{3.38}$$

Dividing both the numerator and denominator by ds and using eq. (3.35), we arrive at

$$v^z = \frac{\tanh\eta_s\sqrt{1 + (\tau u^\eta)^2} + \tau u^\eta}{\sqrt{1 + (\tau u^\eta)^2} + \tau u^\eta\tanh\eta_s}. \tag{3.39}$$

Finally subsituting v^z into eq. (3.37) yields

$$y(\eta_s) = \frac{1}{2}\ln\frac{(\sqrt{1+(\tau u^\eta)^2}+\tau u^\eta)(1+\tanh\eta_s)}{(\sqrt{1+(\tau u^\eta)^2}-\tau u^\eta)(1-\tanh\eta_s)}. \tag{3.40}$$

If τu^η as a function of η_s can be obtained from hydrodynamic simulation, we can use eq. (3.40) to convert between y and η_s.

3.4 Smearing the thermal model

3.4.1 $\frac{dN}{dy}$ from a source at rest

Let's start with a thermal source at rest (i.e. $y = 0$) on the freeze-out surface, where it has a temperature T, volume V and chemical potential μ. For simplicity, we consider classical statistics first. This source will emit particles with different rapidities[5]. To obtain their distribution $\frac{dN}{dy}$, we start from the momentum space distribution in a GCE, i.e., eq. (3.14)

$$\frac{d^3N}{d^3\vec{p}} = \frac{g_s V}{(2\pi)^3} e^{\beta(\mu - E_{\vec{p}})}. \tag{3.41}$$

Here, g_s is the spin degeneracy, which is 1 for scalar bosons such as kaons and pions, and 2 for spin-$1/2$ fermions such as protons and neutrons. Proceeding to determine $\frac{dN}{dy}$, we first notice that $d^3\vec{p} = d^2p_T dp_z$, where $d^2p_T = 2\pi p_T dp_T$ by rotational invariance in the transversal plane. Thus, we have

$$\frac{d^3N}{d^3\vec{p}} = \frac{1}{2\pi}\frac{d^3N}{p_T dp_T dp_z}. \tag{3.42}$$

Then using eq. (3.27), we can identify $p_T dp_T = m_T dm_T$. Finally we replace $p_z = m_T \sinh y$ which gives a Jacobian $dp_z dm_T = m_T \cosh y dm_T dy$. Therefore

$$\frac{dN}{dy} = e^{\beta\mu}\frac{g_s V}{(2\pi)^2}\int_m^\infty dm_T m_T^2 e^{-\beta m_T \cosh y}. \tag{3.43}$$

[5]Not to be confused to the rapidity of the thermal source.

The integral gives

$$\frac{dN}{dy} = \frac{g_s V T^3}{(2\pi)^2} e^{\beta(\mu - m\cosh y)} \frac{2 + 2\beta m \cosh y + (\beta m \cosh y)^2}{\cosh^2 y}. \tag{3.44}$$

We note that we have used the Boltzmann distribution in derivation above, which is only valid when $m \gg T$. As the typical freeze-out temperature of a QGP is $\sim 150\ \mathrm{MeV}$ and bosons have comparable masses ($140\ \mathrm{MeV}$ for pions and $493\ \mathrm{MeV}$ for kaons), in practice it is an inaccurate approximation. As a result, we need to use quantum statistics. Using eq. (3.8) and the fact that $\frac{dN}{dy}$ is linear in the distribution function f we started with, we realised that for bosons,

$$K_B(y; T, V, \mu) \equiv \left(\frac{dN}{dy}\right)_{\text{boson}} = \sum_{n=1}^{\infty} K(y; T/n, V, \mu), \tag{3.45}$$

where as $K(y; T, \mu, V)$ denotes $\frac{dN}{dy}$ in the classical case given by the eq. (3.44). Similarly for fermions

$$K_F(y; T, V, \mu) \equiv \left(\frac{dN}{dy}\right)_{\text{fermion}} = \sum_{n=1}^{\infty} (-1)^{n-1} K(y; T/n, V, \mu). \tag{3.46}$$

3.4.2 Convolution integral

Now we come to the case where we have a source with a rapidity y_0. To obtain the rapidity distribution in this case, we can use Lorentz transformation to boost this source back to its rest frame. By the additivity of rapidity, the boost is simply achieved by replacement $y \to y - y_0$. Precisely, in the boosted frame where the source is at rest, one can use eq. (3.44), and to boost it back, we just replace y in eq. (3.44) by $y - y_0$. Therefore in this case,

$$\begin{aligned} K(y - y_0; T, \mu, V) &\equiv \left(\frac{dN}{dy}\right)_{\text{source at } y_0} \\ &= \frac{g_s V T^3}{(2\pi)^2} e^{\beta(\mu - m\cosh(y - y_0))} \frac{2 + 2\beta m \cosh(y - y_0) + (\beta m \cosh(y - y_0))^2}{\cosh^2(y - y_0)}. \end{aligned} \tag{3.47}$$

Now if we have sources at every rapidity point y with all different thermodynamics as $T(y), \mu(y), V(y)$, it is clear that the final distribution will be

$$\frac{dN}{dy} = \int dy_0 K(y - y_0; T(y_0), \mu(y_0), V(y_0)). \tag{3.48}$$

Depending on the nature of the considered particle, in practice we need to change K above by K_B or K_F. We try to reproduce the particle yields $\frac{dN}{dy}$ by 2 methods

1. Smearing model: This is new in this thesis and the related work [7]. We use some ansatzs for $T(y), V(y), \mu(y)$ and tuning the parameters in the ansatzs so that the final yields are reproduced by eq. (3.48). This method, however, can never give a perfect fitting. In our practice, the fitting is stopped when only a little improvement can be made, and the final global error is less than 10^{-3}, discussed in chapter 4.

2. Discrete model: This is used in a number of papers on rapidity scan, see, e.g. [56]. In this model we treat $\frac{dN}{dy}$ at each y point independently as particle numbers given by eqs. (3.14) and (3.17), so we can calculate (T, V, μ) at each point using fig. 3.1 and eqs. (3.19) and (3.23). This approach makes discrete model always gives exact results for the thermodynamics (T, μ, V) if particle numbers are given as exact. However, as earlier discussed, the starting point of treating each y point independently lacks justification, since particle numbers given by eqs. (3.14) and (3.17) are not $\frac{dN}{dy}$ for a given rapidity, but actually $\int dy \frac{dN}{dy}$, i.e., with y distribution integrated out.

Therefore, also the discrete model is economic to use, one needs to be extra careful with its assumptions, and it is necessary to check if smearing effect is non-negligible when extracting freeze-out thermodynamics. Practically for the smearing model, inferring $T(y), \mu(y), V(y)$ from yields $\frac{dN^\pi}{dy}, \frac{dN^K}{dy}, \frac{dN^{p-\bar{p}}}{dy}$ requires doing a functional fitting, and to proceed, we take the

following ansatz for the functional dependence:

$$T(y) = t_0 + t_2 y^2 + t_4 y^4 + t_6 y^6 + \ldots; \tag{3.49}$$

$$z(y) \equiv e^{\mu(y)/T(y)} - e^{-\mu(y)/T(y)} = z_0 + z_2 y^2 + z_4 y^4 + \ldots \tag{3.50}$$

The reason of using a Taylor expansion for T is that HICs basically explore the top-left part of the QCD phase-transition line where temperature drops rather slowly[6]. A previous study [56] finds indeed that temperature doesn't change significantly for $y \lesssim 3.5$. For z which is related to chemical potential μ and is roughly proportional to net-proton number, due to the decreasing baryon-stopping power at higher beam energy, one also anticipates that it is slowly varying with y. As we go to lower energies, some of these arguments will become less valid. Nevertheless, we included more terms in the expansions so a good fit can be achieved.

For the volume $V(y_s)$ we use a plateau with two half-Gaussian tails:

$$V(y_s) = V_0 \exp\left[-\frac{(|y_s| - y_c)^2}{2\sigma^2} \times \theta(|y_s| - y_c)\right], \tag{3.51}$$

where V_0, y_c, σ are free parameters, controlling the overall scale, the plateau width and the width of the tails.

With the predefined parametrizations, we can now tune the parameters to fit the yields at different beam energies obtained from the hydrodynamic simulation in [7], in order to study the thermodynamics on the freeze-out surface from the smearing thermal model.

[6]When the collision energy is high enough, the fireball doesn't acquire a large baryon chemical potential

Chapter 4

Results and Discussions

In this chapter, we compare the performances and results on extracting the thermodynamics on the freeze-out surface in different models. The chapter starts with a discussion on using the single source model for the beam energy scan. The differences between discrete and smearing thermal models are then considered in section 4.2. We finally compare the thermal models and hydrodynamics simulation in section 4.3. The data here used is identical with ref. [7], which contains particle distribution for net protons, pions and kaons in beam energies $\sqrt{s} = 7.7, 19.6, 62.4$ and 200 GeV per nucleon.

4.1 Single source model: Beam energy scan

Let's first discuss the result from the using the single source model described in section 3.2.2. Varying the collision energy in heavy ion collision, different freeze-out points on the phase diagram can be reached. One then evaluate the multiplicity of for pions, kaons and net protons in experiments.

In our practice, the particle multiplicities are obtained by integrating over rapidity in the yields given in ref. [7], i.e., $N^s = \int dy \frac{dN^s}{dy}$ where $s = \pi, K, p - \bar{p}$. We then follow the procedure given in section 3.2.2, using eqs. (3.18), (3.19) and (3.23) to extract the temperature, baryon chemical potential and volume of the entire fireball. In fig. 4.1, we show

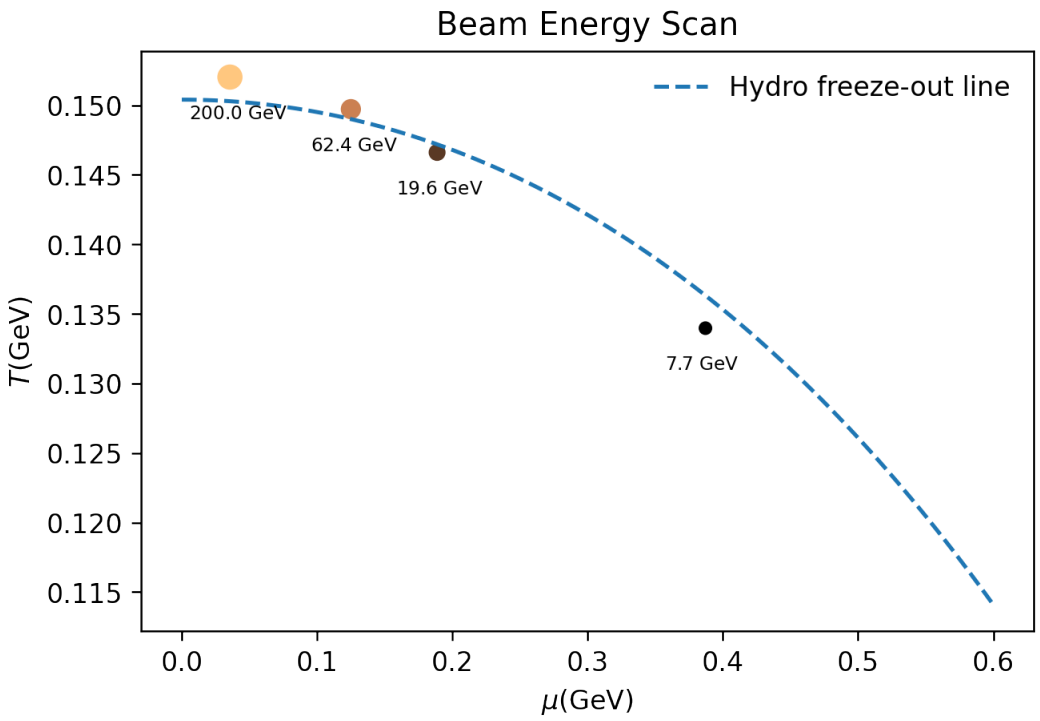

Figure 4.1: Beam energy scan for freeze-out points at different beam energy. Data is from [7], which is identical for the data used later in this chapter. The size of each point is proportional to the volume obtained by eq. (3.19)

the freeze-out points for collisions at $\sqrt{s} = 7.7, 19.6, 62.4$ and 200 GeV. Generally speaking, we observe that when collision energy decreases, the freeze-out point moves to the bottom-right position on the phase diagram. For $\sqrt{s} = 62.4$ and 19.6 GeV, their corresponding points are closer to the freeze-out line used in the hydrodynamic simulation.

The increasing μ_B as we go to lower energy can be partly attributed to the increased baryon stopping power in low-energy collisions [77, 78]. This is relates to the fact that nucleons are "transparent" in ultra high energy collisions. In the ultra-relativistic cases the collided nucleons mostly pass each other, leaving almost no nucleus, and thus little μ_B in the fireball region. This transparency decreases as $\sqrt{s}$ decreases, therefore more nuclei are stopped and join the fireball, a phenomena referred to as baryon stopping [79]. As baryon charge is conserved, the stopped nuclei at the initial stage finally manifest themselves as a larger μ_B on the freeze-out surface.

4.2 Extracting freeze-out thermodynamics by discrete and smearing thermal models

With beam energy scan discussed, we now turn to another strategy of mapping freeze-out points on the phase diagram: rapidity scan. In this section, we compare the performance from thermal models with and without smearing effect, whose frameworks are discussed in section 3.4. Here hydrodynamic yields are from ref. [7] as the previous section.

4.2.1 19.6 GeV

Let's first look at the collision at $\sqrt{s} = 19.6\ \mathrm{GeV}$. We implement both discrete and smearing thermal models on the data. In fig. 4.2, we showed how well our smearing thermal model can reproduce the yields. It is observed that our smearing thermal model repro-

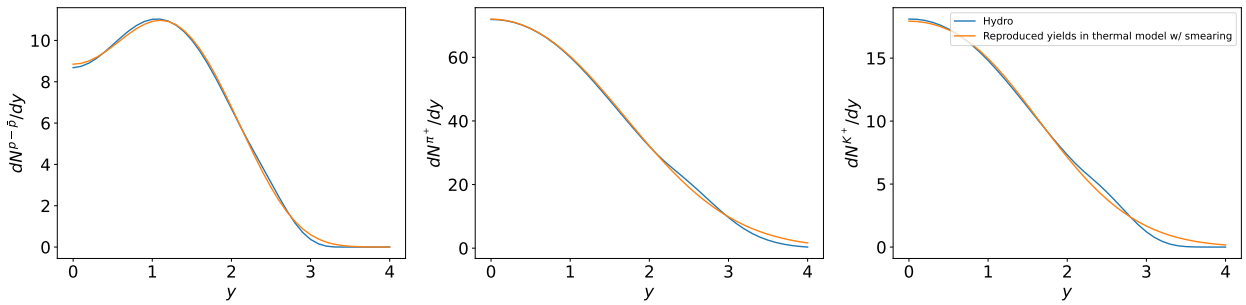

Figure 4.2: Hydrodynamic and smearing thermal model yields at $\sqrt{s} = 19.6\ \mathrm{GeV}$. The panels are for net proton ($p - \bar{p}$), pion (π) and kaon (K) yields, from left to right. In each panel, the blue line is the yields form hydrodynamic simulation which is fitted by the smearing thermal model showed by the orange line.

duces yields well around mid-rapidity, while for the tail ($y \gtrsim 2$), the matching is not so optimal. As we will point out later, the disagreement at the tail is not a significant shortcoming of the model. Because of the usage of parameterisation, this model never gives a perfect fitting while for discrete thermal model, everything is determined analytical through eqs. (3.18), (3.19) and (3.23) so exact results are always given. Therefore,

when compare these two models, one should always keep in mind that the discrepancy between extracted (T, μ, V) are from both:

- intrinsic nature: model differences between discrete and smearing thermal model;
- mismatch in fitting: the discrepancy between hydrodynamic and reproduced yields by smearing thermal model.

If we just want to compare the two models, one way to eliminate the difference from the mismatch is to use discrete thermal model again on reproduced yields from smearing thermal model. In fig. 4.3, we demonstrate this by plotting the extracted thermodynamics from using the discrete thermal model on original hydrodynamic yields (dashed blue line), the smearing thermal model on original hydrodynamic yields (green line) and the discrete thermal model on reproduced yields from smearing thermal model (orange line).

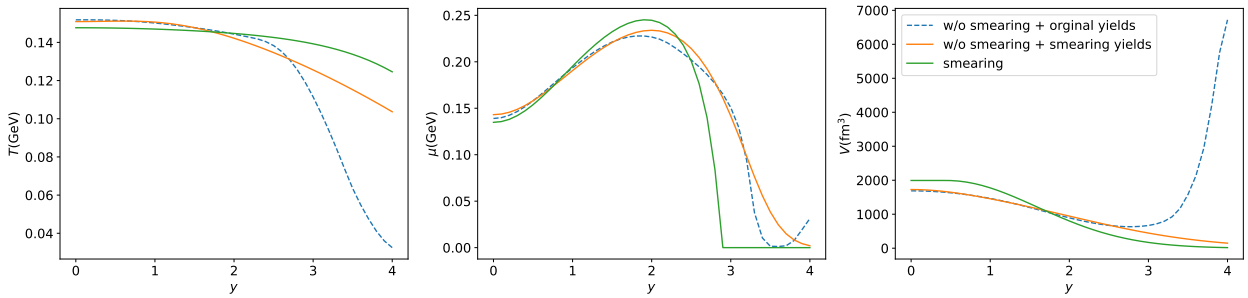

Figure 4.3: Thermodynamic profiles from different thermal models at $\sqrt{s} = 19.6\,\mathrm{GeV}$. The panels are for temperature T, baryon chemical potential μ and volume V as a function of rapidity y respectively, from left to right. In each panel, the orange line corresponds to the profiles extracted by the discrete source model using the particle yields given by the smearing thermal model, i.e., the orange lines in fig. 4.2.

From fig. 4.3 it is shown that around mid rapidity ($y \lesssim 2$), the orange and dashed blue lines match well, indicating that the discrepancy between two models are mostly because of the intrinsic difference between models. A lower temperature is indeed observed by the smearing thermal model. The difference, however, is less than 5%, and the same is

true of baryon chemical potential $\mu(y)$. The only significant difference between the two models around mid-rapidity is the volume $V(y)$, where smearing thermal model gives a volume that is general $\gtrsim 10\%$ than the discrete thermal model. However, comparing the green and orange line which are different thermal models for same yields, the overall system size is still preserved although the volume rapidity distributions are different between two models.

Let's now focus on the discrepancy near the tail. For temperature, the difference between the dashed blue line and the orange line is very significant, indicating a mismatch between reproduced and original hydrodynamic yields in pions and kaons, as one sees from fig. 4.2. On one hand, this is because of the usage of ansatz eqs. (3.49) and (3.51) and is thus unavoidable. On the other hand, as one noticed that in fig. 4.2, the mismatch in yields is not as significant as the discrepancy in temperature profile, this is due to the nature of the discrete model. Let's introduce a short-hand notation n^π, n^K for $\frac{dN^\pi}{dy}, \frac{dN^K}{dy}$, and $\delta n^\pi, \delta n^K$ as their error[1] . Since temperature is uniquely determined by the $\pi-$K ratio, the error in temperature extracted in discrete thermal model is given by

$$\delta T = \frac{dT}{dr_{\pi/K}} \delta \left(\frac{n^\pi}{n^K} \right) = \frac{dT}{dr_{\pi/K}} \frac{n^K \delta n^\pi - n^\pi \delta n^K}{(n^K)^2}. \tag{4.1}$$

A numerical calculation for the first coefficient $\frac{dT}{dr_{\pi/K}}$ is given by fig. 4.4, and is of $O(0.01\ \mathrm{GeV})$ in our range of interests. However, as we approach the tail, as $n^K \to 0$ for $y \gtrsim 3$, since δn^π and δn^K are still finite, δT grows unavoidably. In real experiments, since only a small set of data points for $\frac{dN}{dy}$ is available, one has to do fitting to get a continuous curve for $\frac{dN}{dy}$ to implement the discrete thermal model, an even larger uncertainty would be expected.

In short, at the tail, the discrete thermal model will be too sensitive to any kind of uncertainties we introduced when analysing the data. Although such a quantitative error analysis for smearing thermal model is difficult, given their similar nature, we shouldn't

[1]Can be attributed to either the uncertainties in experimental measurements when using the model directly to experimental data, or fitting error to the hydrodynamic yields as what we are currently focusing on in this section.

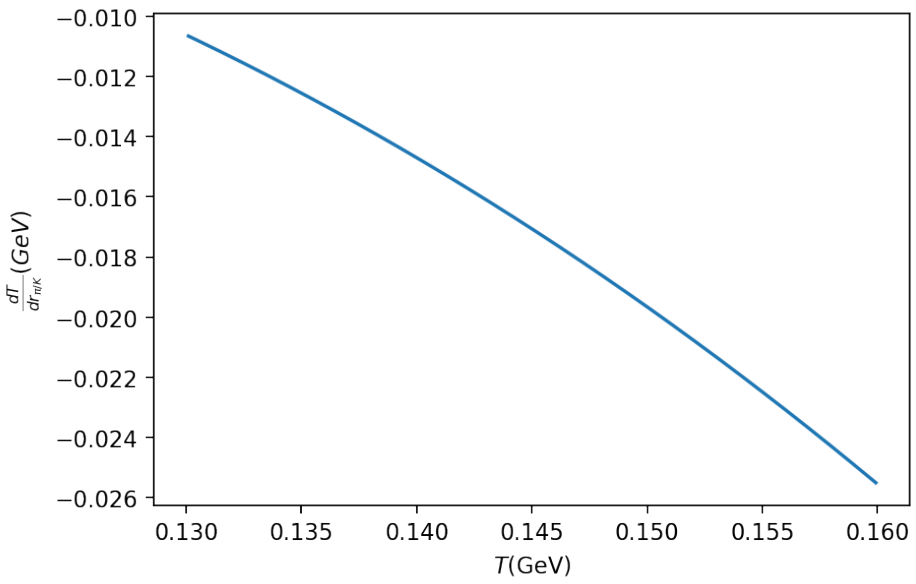

Figure 4.4: $\frac{dT}{dr_{\pi/K}}$ as a function of temperature. As there is an enhancement for large temperature, it's generally of the order of 0.01 GeV.

expect neither the discrete or smearing thermal model to work well in the tail. In chapter 5, we indeed find a similarly large uncertainty smearing thermal model at the tail region by using a Bayesian analysis.

Finally let's move on to the phase diagram. In fig. 4.5, we compare the freeze-out points on the freeze-out surface (later referred as freeze-out point for short) extracted from two thermal models, and compare them with the freeze-out line used in this hydrodynamic simulation[2].

From the phase diagram, we can tell some other advantages of smearing thermal model is that unphysical bottom-left region is avoided, while discrete model has points in that region with a large volume. This can be partly explained by the predefined ansatz in $V(y)$ which requires the volume automatically approaches 0 as we go to larger rapidity. What's more, freeze-out points extracted form smearing thermal model are generally

[2]In ref. [7], the freeze-out in the hydrodynamic simulation is defined a constant energy density $e_{\rm fo} = 0.26\ \mathrm{GeV/fm^3}$, where hydrodynamic language is translated to particle language using the Cooper-Frye prescription described in section 2.2. (T, μ) relation, which is the freeze-out line plotted in fig. 4.5 and other phase diagrams in this chapter, is obtained by the QCD equation of state used in the simulation with this given energy density.

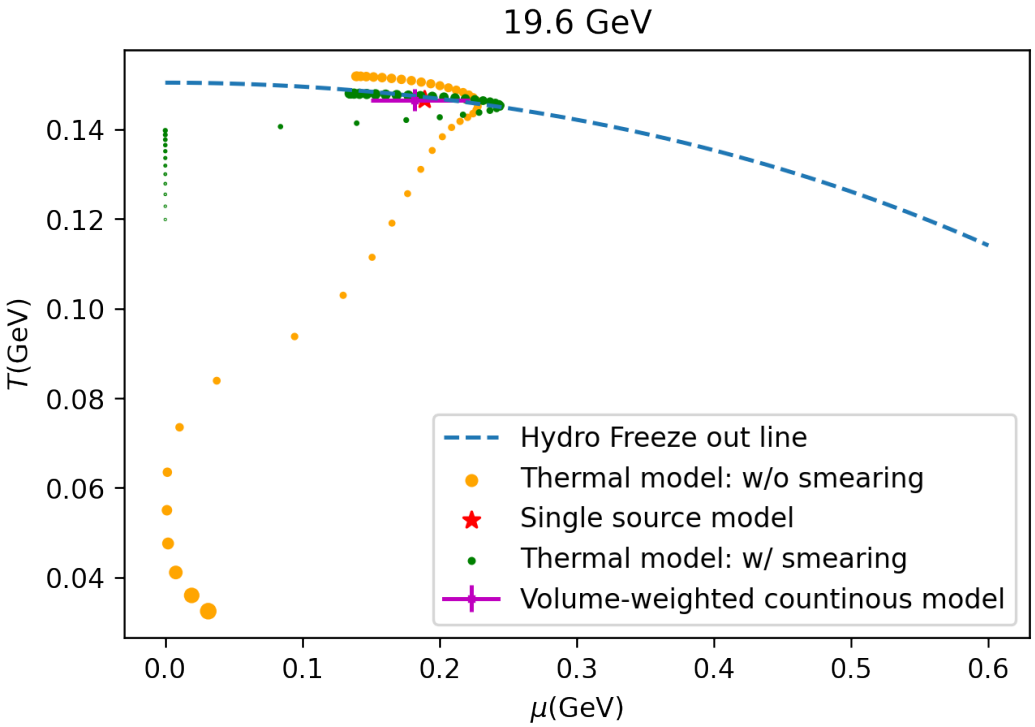

Figure 4.5: Freeze-out points on the phase diagram for $\sqrt{s} = 19.6$ GeV. The dashed blue line is from the freeze-out condition used in hydrodynamic simulation, while the green, orange points are obtained by smearing and discrete thermal models respectively. Here the size of the points is proportional to volume $V(y)$. The red star shows the result from the single source model in fig. 4.1 for this energy.

closer to the freeze-out line used in the hydrodynamic simulation, suggesting a better performance in extracting freeze-out thermodynamics when using the smearing thermal model on data than the discrete model. This is partly because in hydrodynamic simulations smearing effect is automatically taken care of by the Cooper-Frye prescription, and smearing thermal model describes better what really happens on the freeze-out surface.

4.2.2 Lower energy: 7.7 GeV

In fig. 4.6 we compare the reproduced yields from the smearing thermal model and the hydrodynamic simulation. As one can see the fitting is satisfactory. In fig. 4.7 we showed the extracted (T, μ, V) as a function of y. Similar to our 19.6 GeV case, a match between

the orange line and dashed blue line indicates a good fitting is indeed reached by the smearing thermal model around mid rapidity $y \lesssim 1.5$. Again, in trustworthy region of smearing thermal model, a lower temperature is given but the difference is less than $\sim 5\%$. The creeping discrepancy for the tail verifies our statement that the discrete thermal model is too sensitive to any level of uncertainty in $\frac{dN}{dy}$.

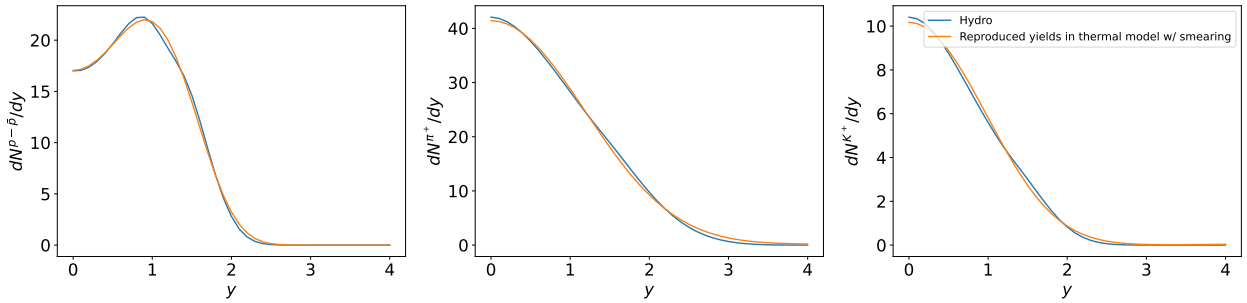

Figure 4.6: Hydrodynamic and smearing thermal model yields at $\sqrt{s} = 7.7\,\mathrm{GeV}$. The panels are for net proton ($p - \bar{p}$), pion (π) and kaon (K) yields, from left to right. In each panel, the blue line is the yields form hydrodynamic simulation which is fitted by the smearing thermal model showed by the orange line.

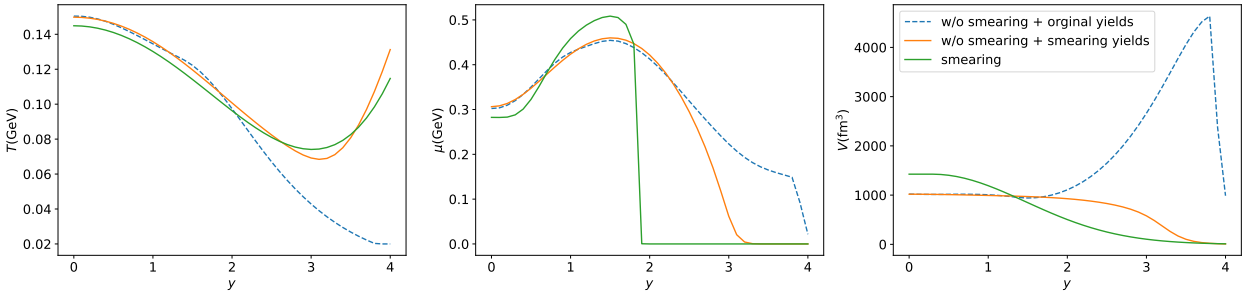

Figure 4.7: Thermodynamic profiles from different thermal models at $\sqrt{s} = 7.7\,\mathrm{GeV}$. The panels are for temperature T, baryon chemical potential μ and volume V as a function of rapidity y respectively, from left to right. In each panel, the orange line corresponds to the profiles extracted by the discrete source model using the particle yields given by the smearing thermal model, i.e., the orange lines in fig. 4.6.

On the phase diagram fig. 4.8, it is shown that freeze-out points in both models gives a wider distribution than what we have already seen for 19.6 GeV. This could be attributed to the stronger baryon stopping power in low-energy collision, where a larger

μ_B is reached in some spatial regions. Other facts such as discrete thermal model gives points far from the freeze-out line and gives unphysical points with large volume in the bottom-left region of the phase diagram, are still similar with what we have for 19.6 GeV.

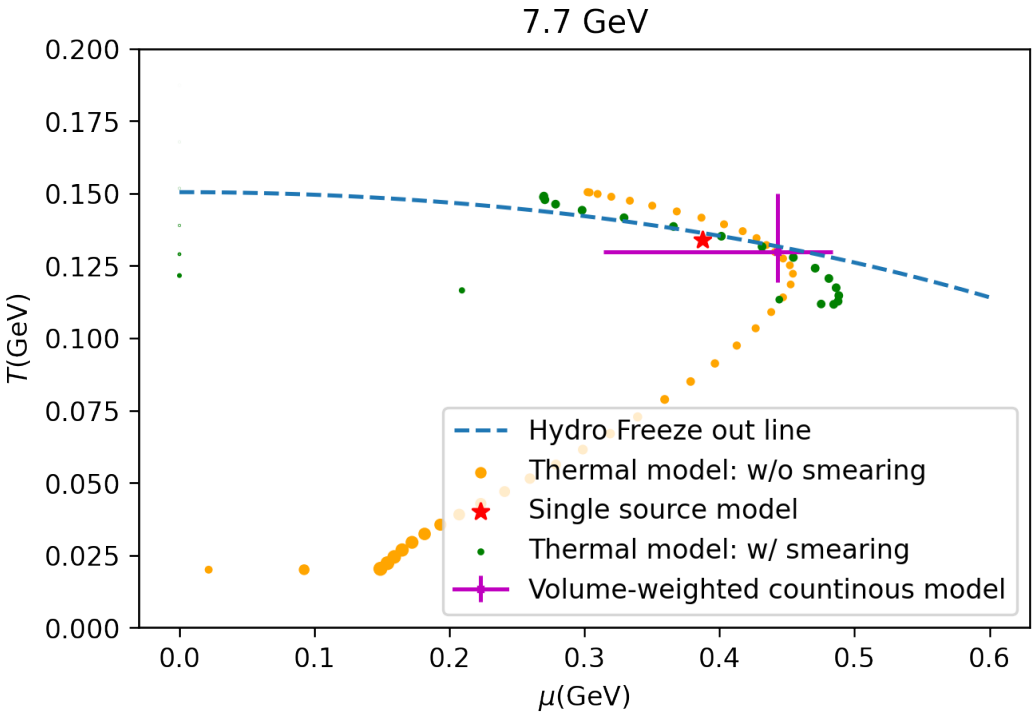

Figure 4.8: Freeze-out points on the phase diagram for $\sqrt{s} = 7.7\,\mathrm{GeV}$. The dashed blue line is from the freeze-out condition used in hydrodynamic simulation, while the green, orange points are obtained by smearing and discrete thermal models respectively. Here the size of the points is proportional to volume $V(y)$. The red star shows the result from the single source model in fig. 4.1 for this energy.

4.2.3 Higher energies: 62.4 and 200 GeV

Now we move ahead to the discussion on higher energies. Similarly we start with comparing the reproduced yields with the hydrodynamic simulation in figs. 4.9 and 4.10. As we see good matches are reached for both energies, we compare the thermodynamics in figs. 4.11 and 4.12.

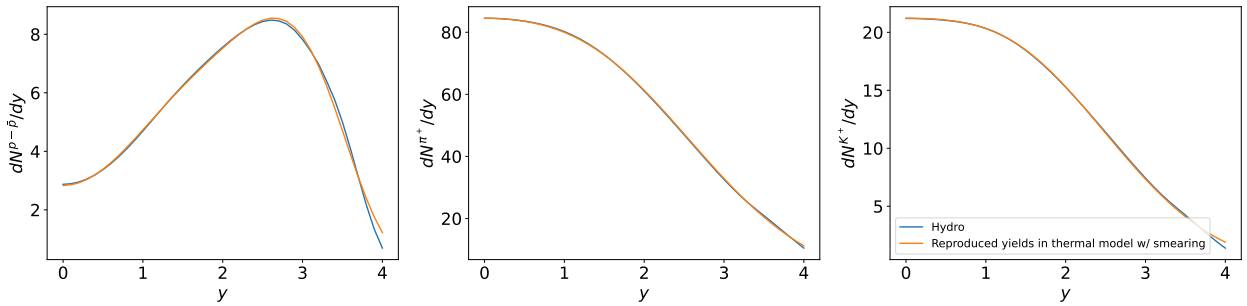

Figure 4.9: Hydrodynamic and smearing thermal model yields at $\sqrt{s} = 62.4\,\mathrm{GeV}$. The panels are for net proton ($p - \bar{p}$), pion (π) and kaon (K) yields, from left to right. In each panel, the blue line is the yields form hydrodynamic simulation which is fitted by the smearing thermal model showed by the orange line.

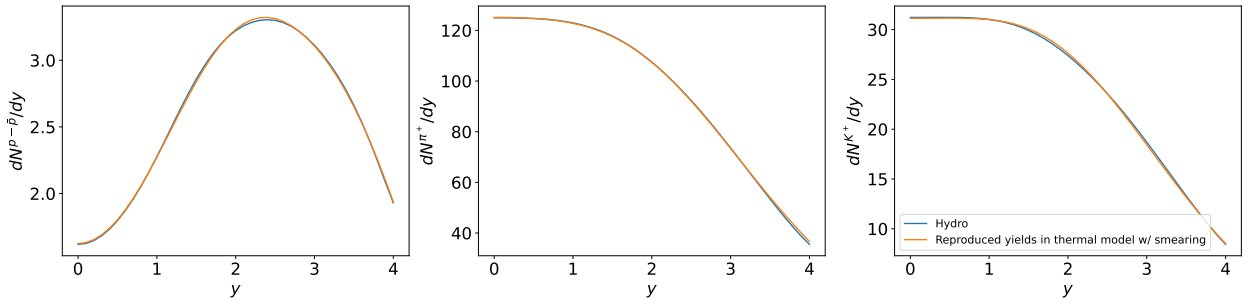

Figure 4.10: Hydrodynamic and smearing thermal model yields at $\sqrt{s} = 200\,\mathrm{GeV}$. The panels are for net proton ($p - \bar{p}$), pion (π) and kaon (K) yields, from left to right. In each panel, the blue line is the yields form hydrodynamic simulation which is fitted by the smearing thermal model showed by the orange line.

One clear trend when beam energy increases is that the system tends to be more isothermal. As the extreme case in 200 GeV, in the rapidity region that we are considering, $145\,\mathrm{MeV} < T < 155\,\mathrm{MeV}$. Such a small variation in temperature gives a smaller model difference between smearing and discrete thermal model, as one can prove that for an exactly homogeneous system, two models give identical result. It is also worth noticing that the unphysically large $V(y)$ is automatically avoided for both 62.4 and 200 GeV. This is partly because the kaon yields are finite for the whole rapidity region $0 < y < 4$, the uncertainty given by eq. (4.1) remains small. In other words, based on our experiences with the other cases, unphysically large $V(y)$ in the discrete thermal model only

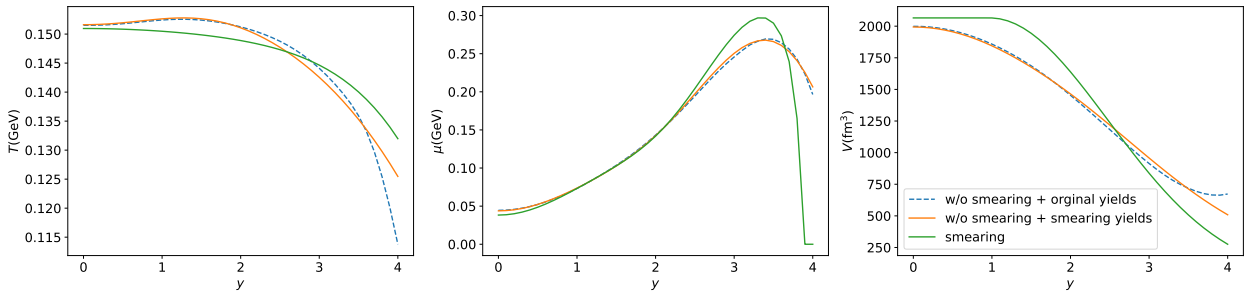

Figure 4.11: Thermodynamic profiles from different thermal models at $\sqrt{s} = 62.4\,\mathrm{GeV}$. The panels are for temperature T, baryon chemical potential μ and volume V as a function of rapidity y respectively, from left to right. In each panel, the orange line corresponds to the profiles extracted by the discrete source model using the particle yields given by the smearing thermal model, i.e., the orange lines in fig. 4.9.

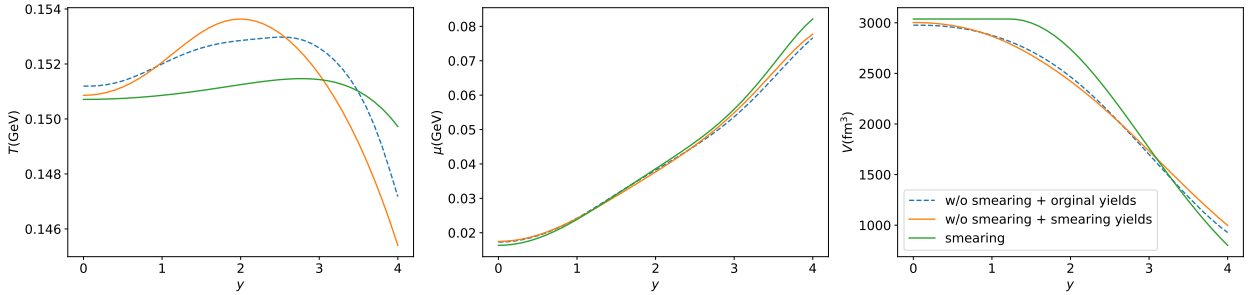

Figure 4.12: Thermodynamic profiles from different thermal models at $\sqrt{s} = 200\,\mathrm{GeV}$. The panels are for temperature T, baryon chemical potential μ and volume V as a function of rapidity y respectively, from left to right. In each panel, the orange line corresponds to the profiles extracted by the discrete source model using the particle yields given by the smearing thermal model, i.e., the orange lines in fig. 4.10.

potentially appears in the tail region, while the tail in this case is yet to be reached within the rapidity interval that we are considering. As one goes to larger y which is not shown here, it is expected that $V(y)$ will still increase in the discrete thermal model. We also see a decreasing baryon chemical potential μ_B for large beam energy. Plotting the freeze-out points on the phase diagrams in figs. 4.13 and 4.14 also verifies our statements above.

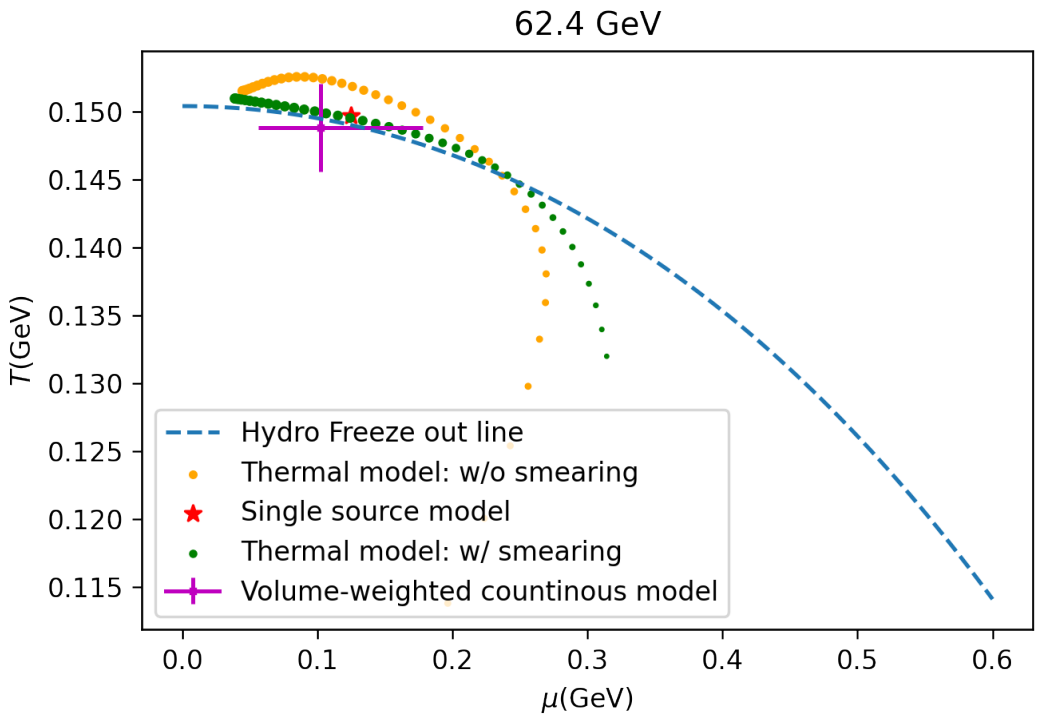

Figure 4.13: Freeze-out points on the phase diagram for $\sqrt{s} = 62.4$ GeV. The dashed blue line is from the freeze-out condition used in hydrodynamic simulation, while the green, orange points are obtained by smearing and discrete thermal models respectively. Here the size of the points is proportional to volume $V(y)$. The red star shows the result from the single source model in fig. 4.1 for this energy.

4.2.4 General discussion for all beam energies

We wrap up this section by a general discussion on all beam energies based on the phase diagram (fig. 4.15). In fig. 4.15 the error bars shows the median, and 25% and 75% percentiles of (T, μ) distributions weighted by volume. To be precise, the $p\%$-volume-weighted percentile of a y-dependent quantity[3] $f(y)$ (denoted as f_p) is obtained from

$$p\% = \frac{\int_{y\, f(y)<f_p} dy f(y) V(y)}{\int_{y=-\infty}^{\infty} dy f(y) V(y)}. \tag{4.2}$$

[3]Here, $T(y)$ or $\mu(y)$.

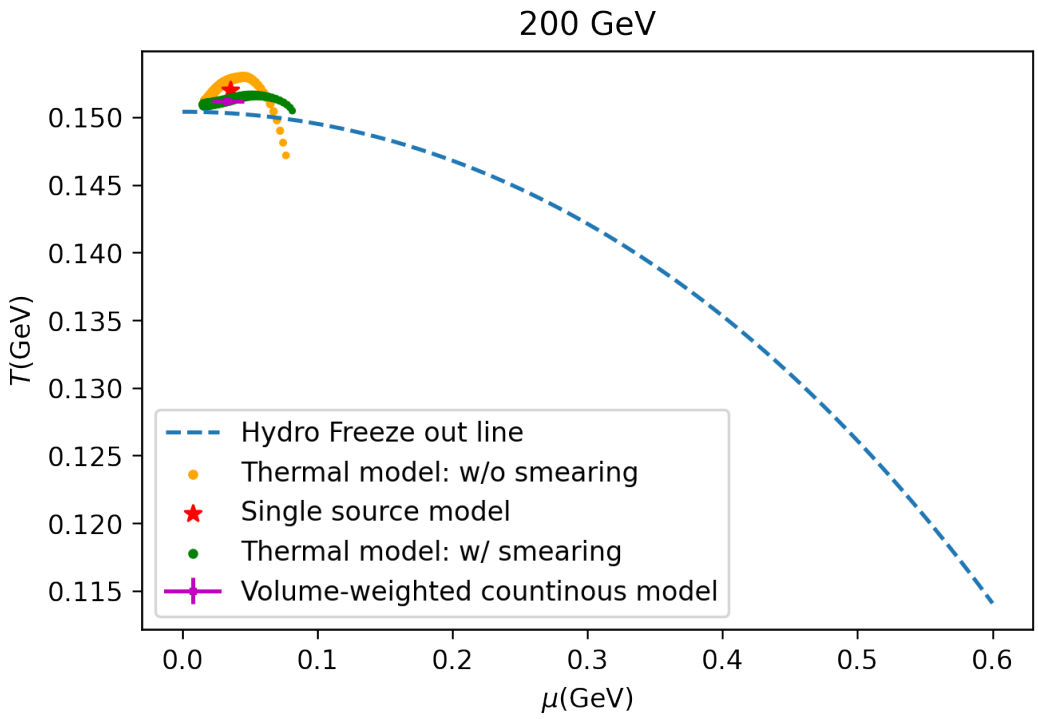

Figure 4.14: Freeze-out points on the phase diagram for $\sqrt{s} = 200$ GeV. The dashed blue line is from the freeze-out condition used in hydrodynamic simulation, while the green, orange points are obtained by smearing and discrete thermal models respectively. Here the size of the points is proportional to volume $V(y)$.The red star shows the result from the single source model in fig. 4.1 for this energy.

The vertical error bar then shows T_{25}, T_{75} on its ends while T_{50} sits at the centre, and similarly for the horizontal error bar. Thus, the length of the error bars at one energy describes the overall distribution of (T, μ) for the freeze-out points extracted by two thermal models.

The reader may notice that in fig. 4.15, the vertical error bars for the discrete model (coloured blue) which represent the distributions of the orange points are not as long as one tells from figs. 4.5, 4.8, 4.13 and 4.14. This is true and is because we performed a cutoff for both models at where volume starts to raise up at the tail in the discrete model in order to avoid super large error bars in the discrete thermal model.

From fig. 4.15, it is clear that as we increase the beam energy, the overall temperature of the freeze-out points goes up while chemical potential goes down, manifesting the $\sqrt{s}$-decreasing baryon stopping power as it is already discussed in section 4.1.

On the other hand, model dependence is observed for every beam energy, where the smearing model typically gives a lower temperature as we've already seen in the discussion of 19.6 GeV. For every beam energy, freeze-out points extracted by the smearing model is closer to the freeze-out line used in hydrodynamic simulation. However we find the model difference decreases as we move to higher and higher energy. As it is already discussed in section 4.2.3, this $\sqrt{s}$-decreasing model difference can be partly explained by the fact that the freeze-out surface is more isothermal for higher beam energy, which is also consistent with by the errors in fig. 4.15.

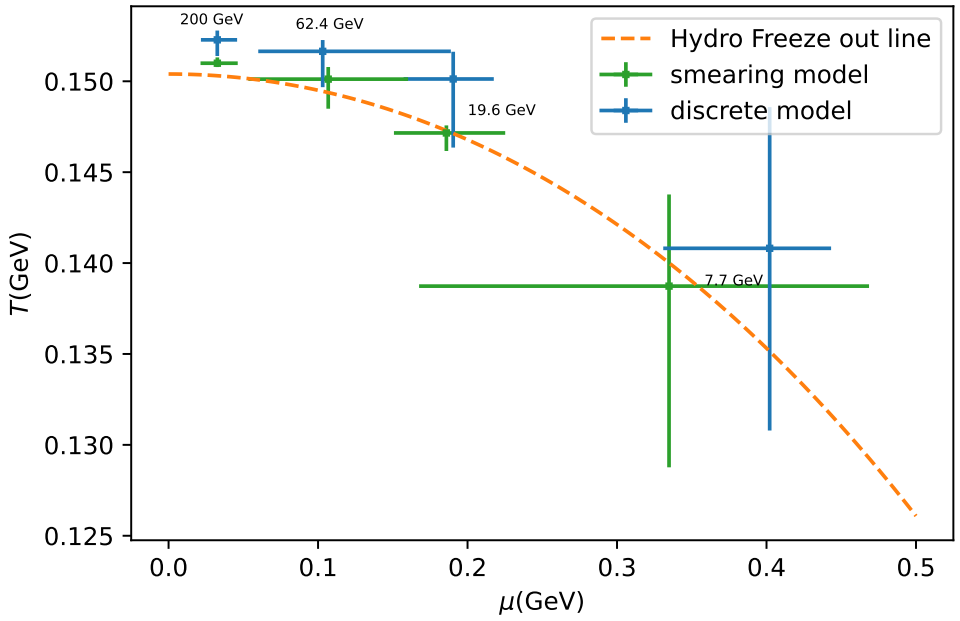

Figure 4.15: Distributions of (T, μ) extracted by two thermal models for different beam energies. The error bars show the median, and 25% and 75% percentiles of (T, μ) distributions weighted by volume. A cutoff is performed to exclude the unphysically large volume at the tails of $\sqrt{s} = 19.6$ and 7.7 GeV.

4.3 Comparing thermal model and Cooper-Frye freeze-out from hydrodynamics simulation

4.3.1 Effects from longitudinal boost

Before comparing on the freeze-out thermodynamic profiles extracted from the thermal models and the hydrodynamic model, let's first discuss how the longitudinal boost affects yields and thermodynamic profiles. As it is mentioned earlier, in hydrodynamic simulation, temperature and chemical potential profiles are built not on rapidity y but space-time rapidity η_s, which is defined in section 3.3.3. Recall that the $y - \eta_s$ conversion eq. (3.40) we obtained there requires $\tau u^{\eta_s}(\eta_s)$ to be known. In fig. 4.16, we showed $\tau u^{\eta_s}(\eta_s)$ for all four energies we used here, obtained from the corresponding hydrodynamic simulation [7]. In general, $\tau u^{\eta_s}(\eta_s)$ tells the strength of longitudinal flow of a fluid cell with a given space-time rapidity η_s. The τu^{η_s} profile is fitted by

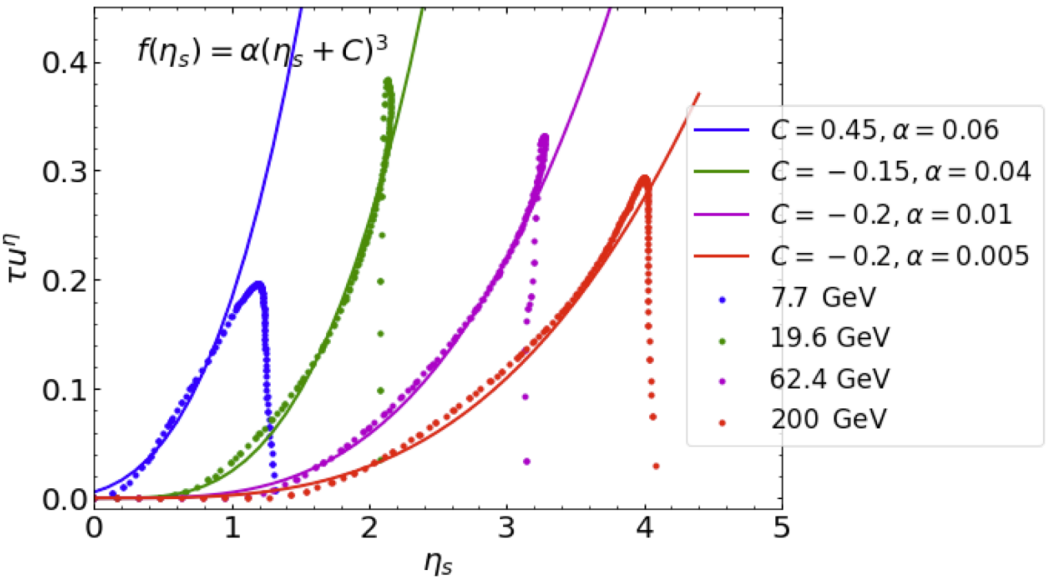

Figure 4.16: $\tau u^{\eta_s}(\eta_s)$ obtained from simulation. Each dot represents $(\eta_s, \tau u^{\eta_s})$ of a freeze-out point, and the solid lines are the cubic fitting for those points. Figure taken from [7].

$$\tau u^{\eta_s}(\eta_s) = \alpha(\eta_s + C)^3 \theta(\eta_s^{\text{cut}} - \eta_s). \tag{4.3}$$

Here θ is the Heaviside step function, α controls the magnitude of longitudinal flows. We notice that, not only hydrodynamic simulation shows the presence of a longitudinal flow, it also shows that there is an η_s cutoff for the freeze-out points, denoted as $\eta_s^{\rm cut}$ in eq. (4.3). This cutoff is however invisible in thermal models.

We hereby focus on $\sqrt{s} = 19.6\,\mathrm{GeV}$. With $\alpha = 0.04$ from hydrodynamic simulation, $y(\eta_s)$ can be found by combining eq. (3.40) and eq. (4.3). Using the same thermodynamic profile $(T(y), \mu(y), V(y))$ in fig. 4.3 obtained earlier from fitting, we obtain the thermodynamic profiles in space-time rapidity by identifying

$$(T(\eta_s), \mu(\eta_s), V(\eta_s)) \equiv (T(y(\eta_s)), \mu(y(\eta_s)), V(y(\eta_s))) \times \theta(\eta_s^{\rm cut} - \eta_s), \tag{4.4}$$

with the cutoff $\eta_s^{\rm cut} = 2.2$ added. This allows us to compare thermal and hydrodynamic models directly in the η_s formulation, which will be later presented in section 4.3.2.

To demonstrate the effects of the longitudinal flow in smearing thermal model, we make α tunable to obtain a new set of $(T(y), \mu(y), V(y))_\alpha$ by

$$(T(y), \mu(y), V(y))_\alpha \equiv (T(\eta_s(y;\alpha), \mu(\eta_s(y;\alpha), V(\eta_s(y;\alpha)). \tag{4.5}$$

Here we explicitly spell out α-dependence of $\eta_s(y;\alpha)$ in the conversion, while quantities on the right-hand-side in terms of η_s is given by eq. (4.4). For each α, we feed the new thermodynamic profile $(T(y), \mu(y), V(y))_\alpha$ to smearing thermal model eq. (3.48) so a new set of yields is obtained, which is showed in fig. 4.17. It is observed in fig. 4.17 that a stronger longitudinal flow can significantly extend the tails in particle yields. As we argued earlier that smearing effects contributes greatly to the tail yields, here we see that the longitudinal flow can be another factor that gives the same contribution. In hydrodynamic simulations, these two factors are automatically taken care of by the Cooper-Frye prescription eq. (2.26). Although the smearing effect can be incooperated into a thermal model as we already did in chapter 3, a thermal model is always built purely on thermodynamics without any information of the kinematics of the fireball. Therefore, although

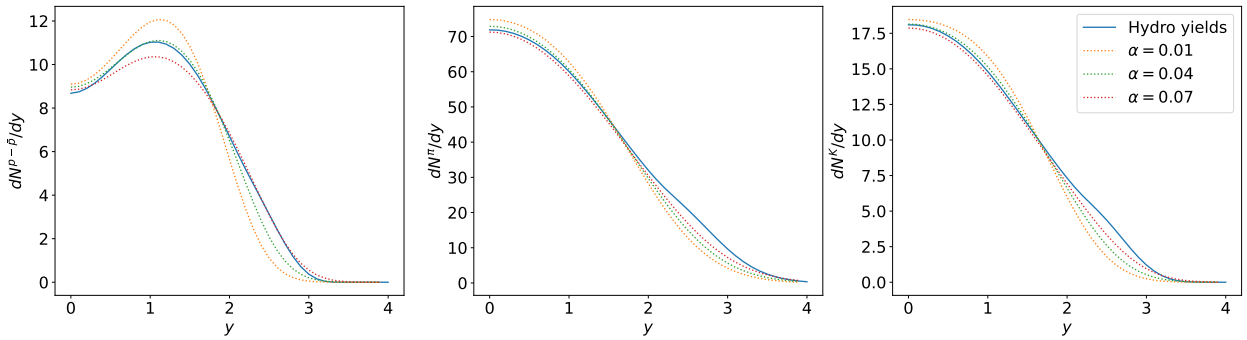

Figure 4.17: Yields from smearing thermal model for different magnitudes of longitudinal flow.

we see from fig. 4.17 that the longitudinal flow can be another contribution for the yields in the tail region, such a contribution, unlike the smearing effect that does the same task, is not considered in any pure thermal model.

4.3.2 Comparing freeze-out thermodynamics between thermal and hydrodynamic models

With the discussion of longitudinal flow done, we are now ready to compare the freeze-out thermodynamics extracted from thermal and hydrodynamic model in the η_s language. We show the result in fig. 4.18, for temperature and chemical potential. Volume profile $V(\eta_s)$ is not extracted from the hydrodynamic simulation, so is not shown here. As one can tell from fig. 4.18, both thermal models deviate from the hydrodynamic model, smearing thermal model does agree better with what is extracted from the hydrodynamic simulation. In general, the difference between the models are still within 10% for the whole η_s range. The large uncertainties we witness before don't show up here because of the η_s cutoff which automatically discards the tail region.

In summary, since all of the three models give similar results in extracting (T, μ) of QGP freeze-out surface with discrepancy $\lesssim 10\%$, we conclude that using thermal model could be an less expensive but still effective way of performing this job instead of running the hydrodynamic simulation, which takes a much longer time to complete. More-

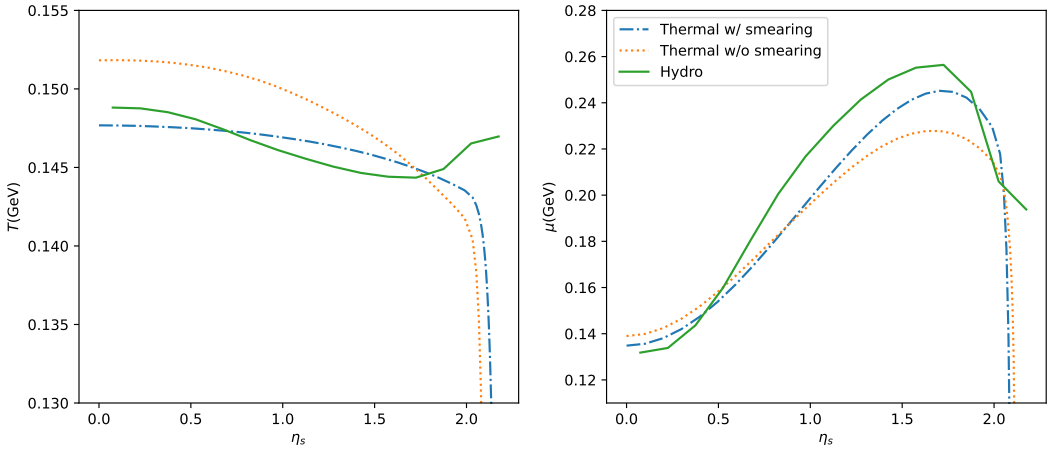

Figure 4.18: Comparison between extracted thermodynamics from smearing thermal model (blue dash-dot lines), discrete thermal model (orange dotted lines) and hydrodynamic simulation (green solid lines).

over, discrete thermal model is also proven to be a simple, fast model for this task with desirable performances at mid rapidity, where the model difference between discrete, smearing thermal model and hydrodynamic simulation is generally within 10%. However, smearing thermal model does give a quantitatively better result, so we expect that considering smearing effect would be still necessary if future experiments cover a wider rapidity range with less errors.

Chapter 5

Thermal model meets experimental data: a Bayesian study on BRAHMS Au+Au collisions at $\sqrt{s} = 62.4\ \mathrm{GeV}$

5.1 Bayesian parameter estimation

Bayesian analysis is a powerful tool to learn from data. It combines both our previous knowledge of the parameters and the constrain from experimental data [80,81]. One of the most important application of Bayesian analysis is the parameter estimation that is to be discussed here and used in the rest of this chapter. It has been proven significantly useful when we have a high-dimensional parameter space. Efforts have been made, for example, to use Bayesian analysis to constrain QCD transport coefficients from experimental data [82, 83], as well as in cosmology [84] and almost every other branch of physics. In this section, we briefly summarize the basic ideas of Bayesian analysis and the techniques of using a Markov Chain Monte Carlo (MCMC) to generate samples from the posterior distribution given by the Bayesian analysis.

The starting point of Bayesian analysis is Bayes' theorem, which relates the conditional probabilities $P(A|B)$ and $P(B|A)$ by

$$P(A|B) = \frac{P(B|A)P(A)}{P(B)}. \tag{5.1}$$

Here, $P(A|B)$ reads "the probability of event A given the fact that event B happened". In the content of a Bayesian parameter estimation, we take $A = \theta$ as the probability distribution of the parameter θ[1], $B = D$ as our data set. In this case, the LHS of eq. (5.1) reads $P(\theta|D)$. The probability distribution of the parameter θ given the data D, is generally called posterior. On the RHS, the likelihood, $P(D|\theta)$ is the probability of having the data to be D with the parameter given to be θ. An unique feature in Bayesian analysis is the presence of the prior, $P(\theta)$, which encodes our previous knowledge about the parameter θ without having the data D. In practice, $P(D|\theta)$ can be easily computed from the model, while $P(\theta)$ can be a rough estimation about the range of θ given our previous knowledge. For example, if our model requires θ to be positive and we can somehow estimate it to be less than b, a feasible choice of prior can be

$$P(\theta) = \begin{cases} \frac{1}{b}, & 0 < \theta < b; \\ 0, & \text{else.} \end{cases} \tag{5.2}$$

Such a prior is called a flat prior. Later in our study, a modified flat prior on a chosen region of the parameter space is also used.

The denominator $P(D)$ in eq. (5.1) is usually regarded as a normalization and thus ignored in most Bayesian studies. In other words, having prior $P(\theta)$ predefined and likelihood $P(D|\theta)$ computed out, it is enough to compute the probability distribution $P(\theta|D)$ without normalization. However, apart from the difficulty when trying to normalize $P(\theta|D)$, in reality, because of the largeness of data set D, the high dimensional

[1]Here we only take the parameter space to be 1-dimensional for simplicity as an introductory illustration, but the generalization to higher dimensional parameter space is straight forward.

parameter space and finally the very complicated analytical expression of the likelihood $P(D|\theta)$, it is unfeasible and usually even impossible to write down the posterior $P(\theta|D)$ in a closed form. Therefore, an algorithm is required to draw samples from this complicated, unnormalized distribution function $P(\theta|D) \propto P(D|\theta)P(\theta)$. One of such sampling algorithms, also the mostly used one, is MCMC with the Metropolis–Hastings (MH) algorithm. Starting from an initial position in the parameter space, MH algorithm generates a Markov Chain that finally converges to the given unnormalized distribution. Having enough samples generated in this way finally allows us to a Monte-Carlo (MC) sampling, which is to approximate the posterior $P(\theta|D)$ by the frequency of the samples.

In summary, the basic workflow of a Bayesian parameter estimation is to have a prior defined based on the previous knowledge, and the likelihood worked out from the model[2]. The posterior probability distribution of the parameter after learning from the data is then worked out using eq. (5.1) with an unknown normalization factor. A MCMC sampling with the MH algorithm can be used to generate samples for that posterior to study the parameter.

5.2 Bayesian study on smearing thermal model

In this section, we perform a Bayesian analysis on extracting the freeze-out thermodynamics by smearing thermal model. Notice that temperature and volume profile $T(y), V(y)$ are fully determined by pion and kaon yields, we first generate samples for $T(y), V(y)$ from measured $\frac{dN^\pi}{dy}$ and $\frac{dN^K}{dy}$ from the BRAHMS experiment [8]. These samples are later used to further generate samples for $\mu(y)$ profile by the net-proton yields $\frac{d^{p-\bar{p}}}{dy}$ measured from the same experiment [9].

[2]In many cases this step is replaced by a Gaussian process emulator trained by the model, which introduces additional uncertainty but greatly reduce the running time of the MC. We don't use the emulator in this thesis since the model running time is not long enough to make an emulator necessary.

5.2.1 $T(y)$ and $V(y)$

Let's first focus on the temperature and volume as a function of rapidity. We inherit the parametrization for $T(y)$ and $V(y)$ previously used as eqs. (3.49) and (3.51). We keep up to y^6 in the Taylor expansion in $T(y)$ so there are 7 parameters in total, which we denote as $\theta = (t_0, t_2, t_4, t_6, V_0, y_c, \sigma_V)$.

Although it is hard to define a prior directly on $t_0, \ldots, t_6$ as the coefficients for higher order terms in the expansion lack a clear physical meaning, a prior can still be defined using the global behaviour of $T(y)$. As a temperature, it must be positive all the time, and should also have an upper bound in the content of a heavy-ion collision, which we conservatively set as $200\ \mathrm{MeV}$. The coefficients should be constrained in such a way that the expected global behaviour of $T(y)$ is respected. Therefore, we define the prior for them as

$$P(t_0, \ldots, t_6) \propto \begin{cases} 1, & \forall y \in (0,4), 0 < T(y; t_0, \ldots, t_6) < 200\ \mathrm{MeV}; \\ 0, & \text{else.} \end{cases} \tag{5.3}$$

On the other hand, for 3 parameters in $V(y)$, V_0 is the volume at mid-rapidity and based on the studies in chapter 4, conservatively it should fall in $10^3 - 10^4\ \mathrm{fm}^3$; y_c is the width of the plateau and should be positive but smaller than the tail observed in yields, so we set $0 < y_c < 4$; σ_V describes how far the tail extends and we assume it is smaller than $2y_c$. A flat prior is then built on these.

Now with the prior defined, let's move on to the discussion of the likelihood $P(D|\theta)$. In the BRAHMS experiment [8, 9], Au+Au collisions were performed at $\sqrt{s} = 62.4\ \mathrm{GeV}$. Here, both $\frac{dN^\pi}{dy}$ and $\frac{dN^K}{dy}$ are measured only for a few y-points around mid-rapidity and at the tail, reported with their errors, demonstrated in fig. 5.2. To obtain the likelihood, we assume that, with given parameters θ, at each rapidity point y_i, the observed $\frac{dN}{dy}$ data follows a Gaussian distribution. This allows us to write down the likelihood as

$$L(\{n_i^s\}; \theta) = \prod_{s=\pi,K} \prod_{i=1}^{n} \frac{1}{\sqrt{2\pi\epsilon_{s,i}^2}} e^{-(n_i^s - n_s(y_i;\theta))^2/2\epsilon_{s,i}^2}. \tag{5.4}$$

Here $s = \pi, K$ refers to boson species, i refers to the index of the experimental data point,

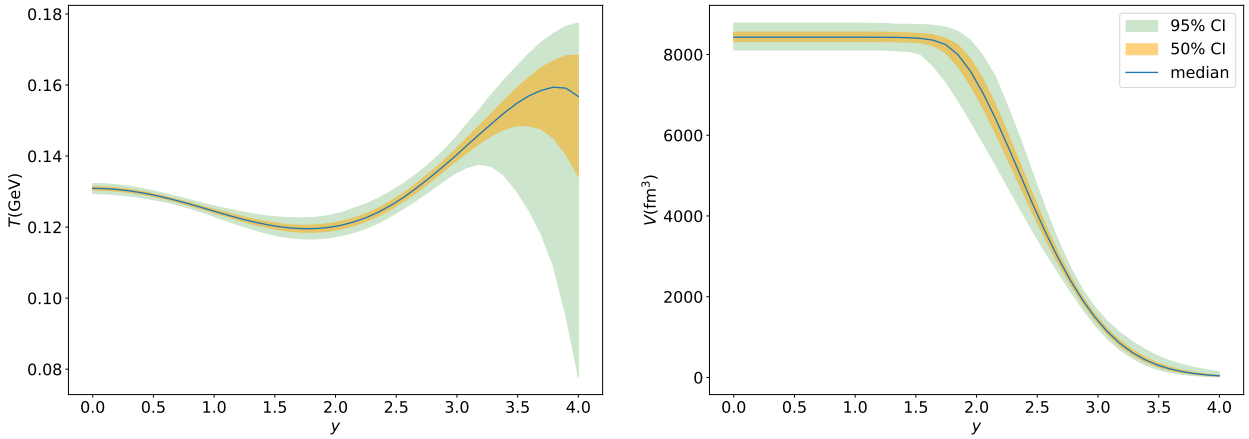

Figure 5.1: Distribution of $T(y)$ and $V(y)$ from the MCMC sampling. Here in each panel, the green-shadowed area refers to the 95% credible interval (CI) while the orange-shadowed for 50% CI. The blue line represents the median of the samples.

$n_s(y_i;\theta) \equiv \frac{dN_s}{dy}(y_i;\theta)$ is a short-hand notation for smearing thermal yields at y_i given the parameter θ and n_i^s is the corresponding experimental measurement, with $\epsilon_{s,i}$ being its error.

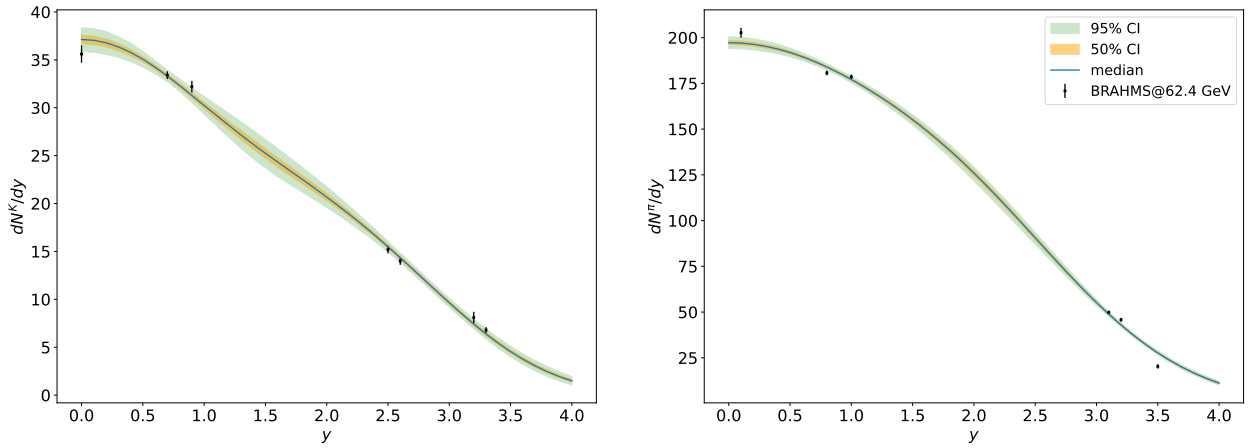

Figure 5.2: Pion and kaon yields in BRAHMS experiment [8] and how they are reproduced by the samples.

An MCMC sampling is then performed to study the distribution of the parameters, which then gives the functional distribution of $T(y)$ and $V(y)$ as we show in fig. 5.1. As our expectation, the uncertainty of extracted temperature greatly increases in the tail

region ($y \gtrsim 3$), similar to the nature of discrete model (eq. (4.1)). However, note that the system size $V(y)$ rapidly goes to zero, such uncertainty may also suggest that the system is not well thermalized in the tail region.

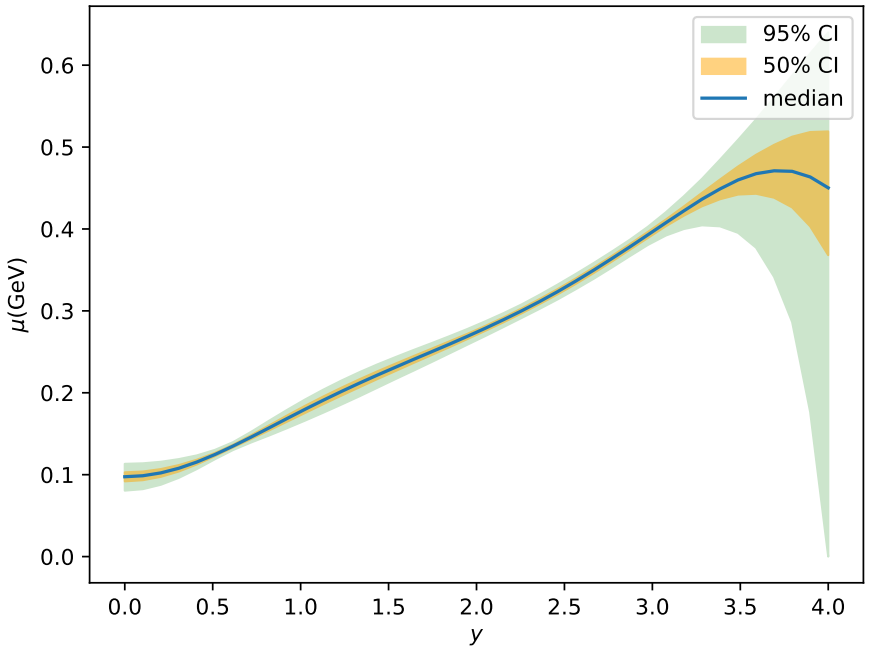

Figure 5.3: Distribution of $\mu(y)$ from the MCMC sampling. Here the green-shadowed area refers to the 95% credible interval (CI) while the orange-shadowed for 50% CI. The blue line represents the median of the samples.

In fig. 5.2, we demonstrate how the samples from the MCMC reproduce the yields measured by the experiment. Despite the paucity of measured data points, it is shown that with the smearing thermal model, the boson yields can be well fitted with little uncertainty. This can be attributed to the usage of both the ansatz and the prior in the parameter space, reflecting an advantage of Bayesian analysis – making use of previous knowledge. We also notice that the large uncertainty in $T(y)$ at the tail doesn't give a significant error in yields at the tail. Because of the vanishing volume in the tail region, sources there give little contribution to yields. This also verifies the fact that yields at the tail are mainly from the mid-rapidity due to the smearing effect.

5.2.2 $\mu(y)$ and the phase diagram

With samples of temperature and volume found by bosons yields, we can now move on to include the net proton yields to draw samples for baryon chemical potential $\mu(y)$. This is done again by using the likelihood defined similarly to eq. (5.4) as

$$L(\{n_i^{p-\bar{p}}\};\theta_z;T(y),V(y)] = \prod_{i=1}^{n} \frac{1}{\sqrt{2\pi\epsilon_i^2}} e^{-\left(n_i^{p-\bar{p}} - n_{p-\bar{p}}(y_i;\theta_z;T(y),V(y))\right)^2/2\epsilon_i^2}. \tag{5.5}$$

Here, the square bracket in $(\{n_i^{p-\bar{p}}\};\theta_z;T(y),V(y)]$ emphasizes that the dependence of L

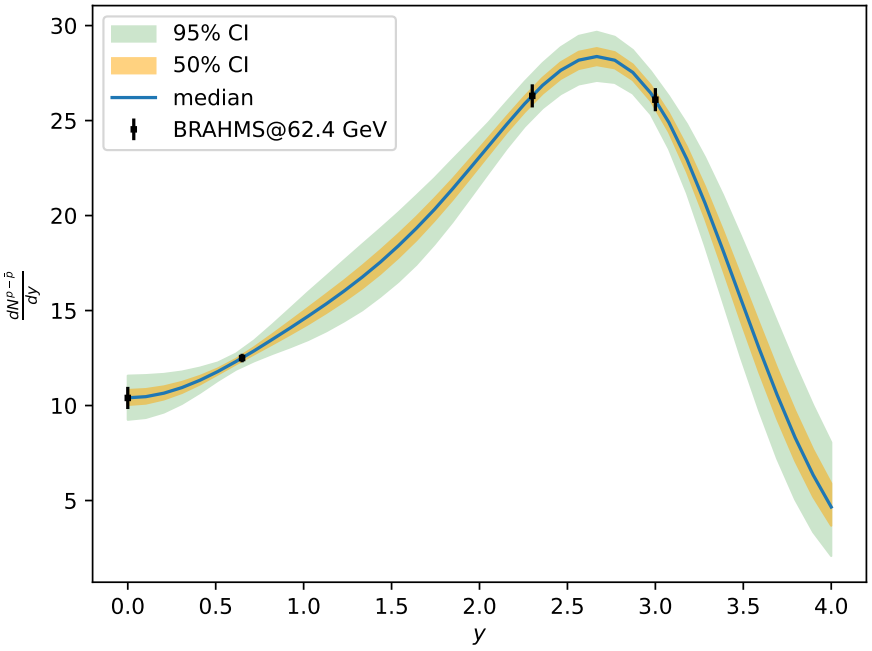

Figure 5.4: Net proton yields in BRAHMS experiment [9] and how they are reproduced by the samples.

and $n_{p-\bar{p}}$ on $T(y)$ and $V(y)$ is functional, i.e. on the entire profiles of T and V as a function of y. $\theta_z = (z_0, z_2, z_4, z_6)$ is the coefficients of the $z(y)$ expansion in eq. (3.49) and are the parameters that we are sampling for with new information on the net-proton yields. Notice that this likelihood requires that $T(y)$ and $V(y)$ are given, we have to draw samples for

θ_z for every sample of $T(y), V(y)$ found previously. Practically, we only randomly drew a small subset of them in order to reduce the number of MCMCs.

On the other hand, unlike T, V, we are hardly able to provide constrains of $z(y)$ from our previous knowledge. Therefore, we simple generate samples using the likelihood eq. (5.5) only, without any prior.

With this setup, we present our results from the MCMC running for the extraction of $\mu(y)$ in fig. 5.3. We again tell that $\mu(y)$ is well constrained except at the tail region, despite of the small number of $\frac{dN^{p-\bar{p}}}{dy}$ available. In fig. 5.4 we show how the samples cover the given data points.

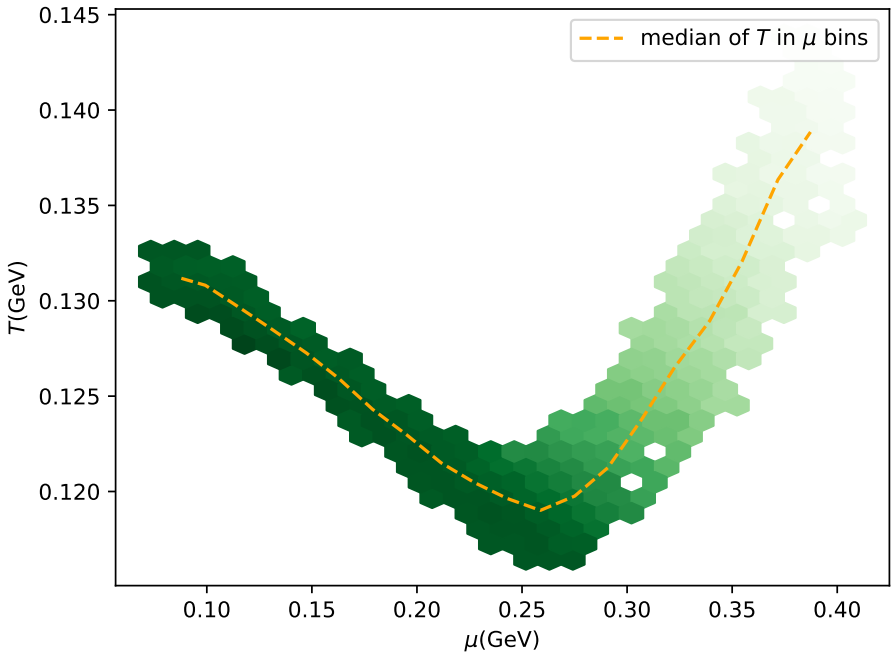

Figure 5.5: Relative distribution of the samples for all freeze-out points with $y < 3$. The darker bin refers to a denser volume-weighted distribution in the bin. The orange dashed line refers to the median value of temperature at given μ.

Finally we turn to the distribution of the samples on the phase diagram. Weighted by the volume $V(y)$ for each point, we demonstrate their relative distribution in fig. 5.5. On one hand, the phase diagram shows that freeze-out points are mainly distributed over

the region of $\mu \lesssim 0.25\,\mathrm{GeV}$, meaning that although in fig. 5.3, samples for $\mu(y)$ go up to $\mu \sim 0.5\,\mathrm{GeV}$ as y increases, those large-rapidity ($y \gtrsim 2$) freeze-out points lack statistical significance because of a rapidly decreasing volume $V(y)$. On the other hand, we found that the sampled temperatures in that dense region are lower than what we found in chapter 4 using the data from hydrodynamic simulation.

One reason for this lower temperature is the final-state particle decay, known as the feed-down effect. In HICs, heavier and unstable particles can decay even after their thermal production at the chemical freeze out, and thus give extra contributions to the final particle yields of lighter mesons and baryons measured experimentally. In a hydrodynamic simulation, this is taken care of by coupling the hydrodynamic evolution with a hadron transport model [66], for example, UrQMD [85]. This is, however, not included in the data used in chapter 4, as the primary goal there is to test pure thermal models [7]. Generally, the feed-down effect creates more pions than kaons, making a $\pi - K$ ratio in the measured distribution higher than Cooper-Frye yields. According to fig. 3.1, such high ratio leads to a lower temperature[3]. There are efforts to include feed-down effect in thermal models, for example, sampling their momenta according to blast wave models [86] and finally letting the resonances decay through all decay chains until only the stable hadrons remain. However, to the best of our knowledge, such efforts are based on discrete (or single source) thermal model.

In summary, the smearing thermal model implemented with a Bayesian analysis shows a good performance in extracting the freeze-out thermodynamics and reproducing the whole profiles of the yields $\frac{dN}{dy}$, even when the yields are only measured at a few points at mid- and large-rapidities. The importance of incorporating feed-down effect into our model is also shown by the lower-than-expected temperature found in our model. Developing a model including both the feed-down effect and the smearing effect would be challenging. We leave it for future work.

[3] Although fig. 3.1 is made based on the discrete thermal model, we expect it to work at least qualitatively for the smearing thermal model we are using now.

Chapter 6

Summary and Outlook

In this thesis, we reviewed the evolution of the fireball produced in a heavy-ion collision. The hydrodynamic description of the fireball in its QGP stage and hadron gas stage before chemical freeze out is also reviewed. We developed a thermal model with the smearing effect to study the thermodynamics on the freeze-out surface, specifically for the temperature T, baryon chemical potential μ and volume V as a function of the rapidity y of each freeze-out point y.

We then used this model to fit rapidity distributions for three particle species, namely net-protons, pions and kaons, which are obtained from a hydrodynamic simulation without feed-down effect. By comparing it with a thermal model without smearing effect, we found that, i) around mid rapidity, two models give quantitatively similar results, while smearing effect slightly lowers the extracted temperature; ii) for large rapidity where particle yields are small, without considering the smearing effect, thermal model gives large uncertainties and unphysical results, which is partly avoided with our smearing thermal model; iii) evidently, particle yields at large rapidity (tail region) are mainly affected given rise by the smearing effect from the mid-rapidity region.

When compared with the freeze-out thermodynamics obtained directly from the used hydrodynamic simulation, results from both thermal models agree with hydrodynamic simulation with error $\lesssim 10\%$, while smearing thermal model display a quantitatively

better result. However, thermal models fail to find the limited system size in the rapidity space as they are blind to any longitudinal dynamics of the freeze-out surface.

The smearing thermal model is then used directly on the data measured from BRAHMS experiment. By performing a Bayesian analysis, we explored the uncertainties in both the reproduced yields and the extracted thermodynamics. Even though the yields $\frac{dN}{dy}$ are only measured for a few rapidity points, the smearing model performs well in reproducing the complete profile of $\frac{dN}{dy}$ with little uncertainties. The uncertainties in extracted freeze-out thermodynamics are found to be small around the mid-rapidity, but increase as we approach the tail, which is qualitatively similar to the case when smearing effect is not taken into account. Because of the prior and ansatz in the thermodynamic profiles, errors in large rapidity region are less significant than thermal model without smearing effect. On the other hand, these errors don't manifest themselves in the reproduced yields, which serves another evidence for the fact that tail yields are mainly own to the smearing effect from the mid-rapidity.

Finally, we need to point out that our smearing thermal model is far from perfect. It works with a predefined parametrization of thermodynamics, which prevents the yields to reach a perfect fit. It also doesn't consider the feed-down effect that changes the yields differently for each particle species after the chemical freeze-out. As a result, the smearing thermal model leads to a lower extracted temperature when applying the model to data obtained from real-world experiments. It would be challenging but also interesting to see how to include both the feed-down effect and smearing effect in the thermal model.

Bibliography

[1] Michael E. Peskin and Daniel V. Schroeder. *An Introduction to quantum field theory*. Addison-Wesley, Reading, USA, 1995.

[2] R. L. Workman et al. Review of Particle Physics. *PTEP*, 2022:083C01, 2022.

[3] A. K. Chaudhuri. *A short course on Relativistic Heavy Ion Collisions*. IOPP, 9 2014.

[4] Akihiko Monnai, Björn Schenke, and Chun Shen. QCD Equation of State at Finite Chemical Potentials for Relativistic Nuclear Collisions. *Int. J. Mod. Phys. A*, 36(07):2130007, 2021.

[5] C. Gale. Private communication, 11 2022.

[6] Pavel Kovtun. Lectures on hydrodynamic fluctuations in relativistic theories. *J. Phys. A*, 45:473001, 2012.

[7] Lipei Du, Han Gao, Sangyong Jeon, and Charles Gale. Rapidity scan with multistage hydrodynamic and statistical thermal models. *arXiv e-prints*, page arXiv:2302.13852, February 2023.

[8] I. C. Arsene et al. Kaon and Pion Production in Central Au+Au Collisions at S(NN)**(1/2) = 62.4 GeV. *Phys. Lett. B*, 687:36–41, 2010.

[9] I. C. Arsene et al. Nuclear stopping and rapidity loss in Au+Au collisions at s(NN)**(1/2) = 62.4-GeV. *Phys. Lett. B*, 677:267–271, 2009.

[10] Murray Gell-Mann. Symmetries of baryons and mesons. *Phys. Rev.*, 125:1067–1084, 1962.

[11] Henry W. Kendall. Deep inelastic scattering: Experiments on the proton and the observation of scaling. *Rev. Mod. Phys.*, 63:597–614, 1991.

[12] E. Eichten, K. Gottfried, T. Kinoshita, J. Kogut, K. D. Lane, and T. M. Yan. Spectrum of charmed quark-antiquark bound states. *Phys. Rev. Lett.*, 34:369–372, Feb 1975.

[13] K. G. Wilson and John B. Kogut. The Renormalization group and the epsilon expansion. *Phys. Rept.*, 12:75–199, 1974.

[14] James M. Cline. *Advanced Concepts in Quantum Field Theory*. SpringerBriefs in Physics. Springer, 10 2020.

[15] Kohsuke Yagi, Tetsuo Hatsuda, and Yasuo Miake. *Quark-gluon plasma: From big bang to little bang*, volume 23. Cambridge University Press, 2005.

[16] N. N. Bogolyubov. On the theory of superfluidity. *J. Phys. (USSR)*, 11:23–32, 1947.

[17] Mark G. Alford, Andreas Schmitt, Krishna Rajagopal, and Thomas Schäfer. Color superconductivity in dense quark matter. *Rev. Mod. Phys.*, 80:1455–1515, 2008.

[18] Edward V. Shuryak. Theory of Hadronic Plasma. *Sov. Phys. JETP*, 47:212–219, 1978.

[19] Edward V. Shuryak. Quantum Chromodynamics and the Theory of Superdense Matter. *Phys. Rept.*, 61:71–158, 1980.

[20] Marek Gazdzicki, Mark Gorenstein, and Peter Seyboth. Brief history of the search for critical structures in heavy-ion collisions. *Acta Phys. Polon. B*, 51:1033, 2020.

[21] Wit Busza, Krishna Rajagopal, and Wilke van der Schee. Heavy Ion Collisions: The Big Picture, and the Big Questions. *Ann. Rev. Nucl. Part. Sci.*, 68:339–376, 2018.

[22] John Bardeen, L. N. Cooper, and J. R. Schrieffer. Microscopic theory of superconductivity. *Phys. Rev.*, 106:162, 1957.

[23] Alexander Altland and Ben D Simons. *Condensed matter field theory*. Cambridge university press, 2010.

[24] Krishna Rajagopal and Frank Wilczek. *The Condensed matter physics of QCD*, pages 2061–2151. World Scientific, 11 2000.

[25] Y. Aoki, G. Endrodi, Z. Fodor, S. D. Katz, and K. K. Szabo. The Order of the quantum chromodynamics transition predicted by the standard model of particle physics. *Nature*, 443:675–678, 2006.

[26] Mari Carmen Bañuls and Krzysztof Cichy. Review on Novel Methods for Lattice Gauge Theories. *Rept. Prog. Phys.*, 83(2):024401, 2020.

[27] Owe Philipsen. The QCD phase diagram at zero and small baryon density. *PoS*, LAT2005:016, 2006.

[28] C. R. Allton, M. Doring, S. Ejiri, S. J. Hands, O. Kaczmarek, F. Karsch, E. Laermann, and K. Redlich. Thermodynamics of two flavor QCD to sixth order in quark chemical potential. *Phys. Rev. D*, 71:054508, 2005.

[29] Philippe de Forcrand, Seyong Kim, and Owe Philipsen. A QCD chiral critical point at small chemical potential: Is it there or not? *PoS*, LATTICE2007:178, 2007.

[30] Lorenzo Dini, Prasad Hegde, Frithjof Karsch, Anirban Lahiri, Christian Schmidt, and Sipaz Sharma. Chiral phase transition in three-flavor QCD from lattice QCD. *Phys. Rev. D*, 105(3):034510, 2022.

[31] A. Bazavov et al. Chiral crossover in QCD at zero and non-zero chemical potentials. *Phys. Lett. B*, 795:15–21, 2019.

[32] Simon Roessner, T. Hell, C. Ratti, and W. Weise. The chiral and deconfinement crossover transitions: PNJL model beyond mean field. *Nucl. Phys. A*, 814:118–143, 2008.

[33] Larry McLerran and Robert D. Pisarski. Phases of cold, dense quarks at large N(c). *Nucl. Phys. A*, 796:83–100, 2007.

[34] Steven Weinberg. *Cosmology*. OUP Oxford, 2008.

[35] Francois Gelis, Edmond Iancu, Jamal Jalilian-Marian, and Raju Venugopalan. The Color Glass Condensate. *Ann. Rev. Nucl. Part. Sci.*, 60:463–489, 2010.

[36] Javier L. Albacete and Cyrille Marquet. Gluon saturation and initial conditions for relativistic heavy ion collisions. *Prog. Part. Nucl. Phys.*, 76:1–42, 2014.

[37] Bjoern Schenke, Prithwish Tribedy, and Raju Venugopalan. Fluctuating Glasma initial conditions and flow in heavy ion collisions. *Phys. Rev. Lett.*, 108:252301, 2012.

[38] Gojko Vujanovic. Electromagnetic probes of the Quark-Gluon Plasma. In *29th International Conference on Ultra-relativistic Nucleus-Nucleus Collisions*, 8 2022.

[39] Charles Gale, Jean-François Paquet, Björn Schenke, and Chun Shen. Multimessenger heavy-ion collision physics. *Phys. Rev. C*, 105(1):014909, 2022.

[40] J. I. Kapusta and Charles Gale. *Finite-temperature field theory: Principles and applications*. Cambridge Monographs on Mathematical Physics. Cambridge University Press, 2011.

[41] Francesco Becattini, Marcus Bleicher, Thorsten Kollegger, Tim Schuster, Jan Steinheimer, and Reinhard Stock. Hadron Formation in Relativistic Nuclear Collisions and the QCD Phase Diagram. *Phys. Rev. Lett.*, 111:082302, 2013.

[42] P. Braun-Munzinger and J. Wambach. The Phase Diagram of Strongly-Interacting Matter. *Rev. Mod. Phys.*, 81:1031–1050, 2009.

[43] P. Braun-Munzinger, J. Stachel, and Christof Wetterich. Chemical freezeout and the QCD phase transition temperature. *Phys. Lett. B*, 596:61–69, 2004.

[44] Chun Shen and Björn Schenke. Dynamical initial state model for relativistic heavy-ion collisions. *Phys. Rev. C*, 97(2):024907, 2018.

[45] Iurii Karpenko. Rapidity scan in heavy ion collisions at $\sqrt{s_{\rm NN}} = 72$ GeV using a viscous hydro + cascade model. *Acta Phys. Polon. B*, 50:141–148, 2019.

[46] F. Becattini, M. Gazdzicki, A. Keranen, J. Manninen, and R. Stock. Chemical equilibrium in nucleus nucleus collisions at relativistic energies. *Phys. Rev. C*, 69:024905, 2004.

[47] A. Andronic, P. Braun-Munzinger, and J. Stachel. Thermal hadron production in relativistic nuclear collisions: The Hadron mass spectrum, the horn, and the QCD phase transition. *Phys. Lett. B*, 673:142–145, 2009. [Erratum: Phys.Lett.B 678, 516 (2009)].

[48] Enrico Fermi. Angular Distribution of the Pions Produced in High Energy Nuclear Collisions. *Phys. Rev.*, 81:683–687, 1951.

[49] L. D. Landau. On the multiparticle production in high-energy collisions. *Izv. Akad. Nauk Ser. Fiz.*, 17:51–64, 1953.

[50] Declan Keane. The Beam Energy Scan at the Relativistic Heavy Ion Collider. *J. Phys. Conf. Ser.*, 878(1):012015, 2017.

[51] Peter Braun-Munzinger, Krzysztof Redlich, and Johanna Stachel. Particle production in heavy ion collisions. pages 491–599, 4 2003.

[52] Abdel Nasser Tawfik. Equilibrium statistical-thermal models in high-energy physics. *Int. J. Mod. Phys. A*, 29(17):1430021, 2014.

[53] A. Andronic, P. Braun-Munzinger, K. Redlich, and J. Stachel. Hadron yields in central nucleus-nucleus collisions, the statistical hadronization model and the QCD phase diagram. In *Criticality in QCD and the Hadron Resonance Gas*, 1 2021.

[54] Bartlomiej Biedron and Wojciech Broniowski. Rapidity-dependent spectra from a single-freeze-out model of relativistic heavy-ion collisions. *Phys. Rev. C*, 75:054905, 2007.

[55] Wojciech Broniowski and Barlomiej Biedron. Rapidity-dependent chemical potentials in a statistical approach. *J. Phys. G*, 35:044018, 2008.

[56] Viktor Begun, Daniel Kikoła, Volodymyr Vovchenko, and Daniel Wielanek. Estimation of the freeze-out parameters reachable in a fixed-target experiment at the CERN Large Hadron Collider. *Phys. Rev. C*, 98(3):034905, 2018.

[57] C. Blume. Centrality and energy dependence of proton, light fragment and hyperon production. *J. Phys. G*, 34:S951–954, 2007.

[58] F. Becattini and L. Tinti. Thermodynamical inequivalence of quantum stress-energy and spin tensors. *Phys. Rev. D*, 84:025013, 2011.

[59] Shuzhe Shi, Charles Gale, and Sangyong Jeon. From chiral kinetic theory to relativistic viscous spin hydrodynamics. *Phys. Rev. C*, 103(4):044906, 2021.

[60] L.D. LANDAU and E.M. LIFSHITZ. Chapter xv - relativistic fluid dynamics. In L.D. LANDAU and E.M. LIFSHITZ, editors, *Fluid Mechanics (Second Edition)*, pages 505–514. Pergamon, second edition edition, 1987.

[61] Bhanuday Sharma and Rakesh Kumar. Estimation of bulk viscosity of dilute gases using a nonequilibrium molecular dynamics approach. *Phys. Rev. E*, 100:013309, Jul 2019.

[62] Ulrich Heinz and Raimond Snellings. Collective flow and viscosity in relativistic heavy-ion collisions. *Ann. Rev. Nucl. Part. Sci.*, 63:123–151, 2013.

[63] P. Kovtun, Dan T. Son, and Andrei O. Starinets. Viscosity in strongly interacting quantum field theories from black hole physics. *Phys. Rev. Lett.*, 94:111601, 2005.

[64] Eric D'Hoker and Daniel Z. Freedman. Supersymmetric gauge theories and the AdS / CFT correspondence. In *Theoretical Advanced Study Institute in Elementary Particle Physics (TASI 2001): Strings, Branes and EXTRA Dimensions*, pages 3–158, 1 2002.

[65] Huichao Song, Steffen A. Bass, Ulrich Heinz, Tetsufumi Hirano, and Chun Shen. 200 A GeV Au+Au collisions serve a nearly perfect quark-gluon liquid. *Phys. Rev. Lett.*, 106:192301, 2011. [Erratum: Phys.Rev.Lett. 109, 139904 (2012)].

[66] Charles Gale, Sangyong Jeon, and Bjoern Schenke. Hydrodynamic Modeling of Heavy-Ion Collisions. *Int. J. Mod. Phys. A*, 28:1340011, 2013.

[67] Sera Cremonini. The Shear Viscosity to Entropy Ratio: A Status Report. *Mod. Phys. Lett. B*, 25:1867–1888, 2011.

[68] Alex Buchel. Bulk viscosity of gauge theory plasma at strong coupling. *Phys. Lett. B*, 663:286–289, 2008.

[69] Peter Brockway Arnold, Caglar Dogan, and Guy D. Moore. The Bulk Viscosity of High-Temperature QCD. *Phys. Rev. D*, 74:085021, 2006.

[70] William A. Hiscock and Lee Lindblom. Linear plane waves in dissipative relativistic fluids. *Phys. Rev. D*, 35:3723–3732, 1987.

[71] W. Israel. Nonstationary irreversible thermodynamics: A Causal relativistic theory. *Annals Phys.*, 100:310–331, 1976.

[72] Pavel Kovtun. First-order relativistic hydrodynamics is stable. *JHEP*, 10:034, 2019.

[73] Fred Cooper and Graham Frye. Comment on the Single Particle Distribution in the Hydrodynamic and Statistical Thermodynamic Models of Multiparticle Production. *Phys. Rev. D*, 10:186, 1974.

[74] M. McNelis and U. Heinz. Modified equilibrium distributions for cooper-frye particlization. *Phys. Rev. C*, 103:064903, Jun 2021.

[75] Akihiko Monnai and Tetsufumi Hirano. Effects of Bulk Viscosity at Freezeout. *Phys. Rev. C*, 80:054906, 2009.

[76] R. K. Pathria. *Statistical Mechanics*. Butterworth-Heinemann, 2nd ed. edition, 1996.

[77] Dhananjaya Thakur, Sunil Jakhar, Prakhar Garg, and Raghunath Sahoo. Estimation of Stopped Protons at Energies Relevant for a Beam Energy Scan at the BNL Relativistic Heavy-Ion Collider. *Phys. Rev. C*, 95(4):044903, 2017.

[78] L. Adamczyk et al. Energy Dependence of Moments of Net-proton Multiplicity Distributions at RHIC. *Phys. Rev. Lett.*, 112:032302, 2014.

[79] Marek Jeżabek and Andrzej Rybicki. Solving the Puzzle of Nuclear Stopping Power. *Acta Phys. Polon. B*, 52(8):981–1005, 2021.

[80] Matthew Heffernan. How about that Bayes: Bayesian techniques and the simple pendulum. *arXiv e-prints*, page arXiv:2104.08621, April 2021.

[81] Udo von Toussaint. Bayesian inference in physics. *Rev. Mod. Phys.*, 83:943–999, Sep 2011.

[82] D. Everett et al. Multisystem Bayesian constraints on the transport coefficients of QCD matter. *Phys. Rev. C*, 103(5):054904, 2021.

[83] Matthew R. Heffernan, Charles Gale, Sangyong Jeon, and Jean-François Paquet. Bayesian quantification of strongly-interacting matter with color glass condensate initial conditions. 2 2023.

[84] Antony Lewis and Sarah Bridle. Cosmological parameters from CMB and other data: A Monte Carlo approach. *Phys. Rev. D*, 66:103511, 2002.

[85] Hannah Petersen, Jan Steinheimer, Gerhard Burau, Marcus Bleicher, and Horst Stöcker. A Fully Integrated Transport Approach to Heavy Ion Reactions with an Intermediate Hydrodynamic Stage. *Phys. Rev. C*, 78:044901, 2008.

[86] Volodymyr Vovchenko and Horst Stoecker. Thermal-FIST: A package for heavy-ion collisions and hadronic equation of state. *Comput. Phys. Commun.*, 244:295–310, 2019.